

Numerical study of broadband sound pulse propagation in three-dimensional oceanic waveguides

Frédéric Sturm^{a)}

*Laboratoire de Mécanique des Fluides et d'Acoustique, UMR CNRS 5509, École Centrale de Lyon,
36 Avenue Guy de Collongue, FR-69134 Ecully Cedex, France*

(Received 22 July 2004; revised 14 December 2004; accepted 15 December 2004)

In this paper, the propagation of a broadband sound pulse in three-dimensional (3D) shallow water waveguides is investigated numerically. Two cases are examined: (i) the 3D ASA benchmark wedge, and (ii) the 3D Gaussian canyon. The numerical method used to solve the four-dimensional acoustic problem is based on a Fourier synthesis technique. The frequency-domain calculations are carried out using the fully 3D parabolic equation based model 3DWAPE, recently modified to include a wide-angle paraxial approximation for the azimuthal component. A broadband sound pulse with a central frequency of 25 Hz and a bandwidth of 40 Hz is considered. For both test cases, 3D results corresponding to a 25 Hz cw point source are first presented and compared with predictions from a 3D adiabatic modal model. Then, the acoustic problem is solved considering the broadband source pulse. The modal structure of the received signals is analyzed and exhibits multiple mode arrivals of the propagating signal. © 2005 Acoustical Society of America. [DOI: 10.1121/1.1855791]

PACS numbers: 43.30.Bp, 43.30.Dr, 43.30.Gv [AIT]

Pages: 1058–1079

I. INTRODUCTION

It has been demonstrated both experimentally^{1–3} and numerically^{4,5} that in some particular oceanic environments, the horizontal refraction of propagating sound waves cannot be neglected and leads, far from the source, to significant three-dimensional (3D) effects. Fully three-dimensional models are needed to predict such 3D effects. Note that in this work, a model is referred to as 3D if it allows horizontal refraction to be considered. Otherwise, the model is said to be two-dimensional (2D), $N \times 2D$, or pseudo-3D. Among existing 3D codes available in the underwater acoustics community,^{6–10} parabolic equation (PE) based models are largely used since they are efficient for solving complex sound propagation problems in various oceanic environments. The reader is referred to Ref. 11 for an exhaustive review of the 3D codes based on modal theory, parabolic equation, rays, and hybrid models, and in particular to Ref. 12 for a specialized review of existing 3D PE models. The main drawback of 3D models in cylindrical coordinates (which is the case for most 3D PE models) is that they are computationally expensive. Indeed, a 3D code is at least two orders of magnitude slower than any $N \times 2D$ code since (i) a very large number of points is required in the azimuthal direction to maintain the necessary arclength between adjacent bearing angles, and (ii) a differential operator with respect to the azimuthal coordinate must be incorporated into the solution. However, rising computer performance as well as the development of efficient numerical techniques^{9,13} allows 3D PE models to be treated at a reasonable computational cost. A calculation in four-dimensional (4D) (i.e., three spatial dimensions and time) using Fourier synthesis methods is thus now possible (at least at low frequencies), allowing the important question of broadband signal dispersion in general 3D waveguides to be addressed.

The aim of this work is to study the propagation of broadband sound pulses in three-dimensional shallow water waveguides. The numerical method used to solve the relevant 4D acoustic problems is based on Fourier synthesis of frequency-domain solutions. The calculations in 3D are done using the 3DWAPE code based on a fully three-dimensional parabolic equation.¹³ Two 3D acoustic problems are treated in this paper. They both consist of an isovelocity water layer overlying a lossy, homogeneous, half-space sedimental layer. They only differ in the description of the bottom geometry. The first acoustic problem considered is a 3D benchmark wedge based on a three-dimensional extension of the original two-dimensional ASA wedge configuration.¹⁴ Preliminary results of broadband sound pulse propagation obtained using 3DWAPE for this specific 3D wedge problem can be found in Ref. 15. They showed that the modal structures of the propagating pulses calculated using a 3D PE model were qualitatively consistent with previous results obtained by Westwood¹⁶ for a similar case using an analytical method. Though these results were satisfying and encouraging, no quantitative comparison with any exact solution was made. Note that in its original configuration, the 3DWAPE code had a very-wide-angle capability along the vertical direction but only a narrow-angle capability along the azimuthal direction. It has recently been modified to handle higher-order paraxial approximations along the azimuthal direction. The results of Ref. 15 were obtained using the azimuthal narrow-angle version of the code. In the present paper, the issue of using wide-angle approximation in azimuth is addressed. In particular, numerical solutions obtained using various paraxial approximations in azimuth are compared with a reference analytical solution based on the image method. Broadband calculations are now carried out using the azimuthal wide-angle version of the code. The second problem considered is the 3D Gaussian canyon test case. It corresponds to a variant of the original 3D Gaussian canyon test case created for the

^{a)}Electronic mail: frederic.sturm@ec-lyon.fr

SWAM'99 Shallow Water Acoustic Modeling Workshop.¹⁷ Results for the original SWAM'99 test case were obtained for a 25 Hz cw point source.^{7,18} Modifications have been made such that only three propagating modes exist at the source position (as in the 3D benchmark wedge) which makes the modal structure analysis of the received signals easier. Note that in its original form, eleven propagating modes were present. The problem involving a broadband sound pulse is analyzed with the same methodology as for the 3D wedge problem.

The organization of this paper is as follows: In Sec. II, the Fourier synthesis technique is briefly summarized, and the 3DWAPE model is presented. Its wide-angle azimuthal capability is discussed; a review of the existing 3D PE code is also given. In Sec. III, the two acoustic shallow water problems are described. For both test cases, a broadband source pulse with a central frequency of 25 Hz and a bandwidth of 40 Hz is considered. The 3D ASA benchmark problem is studied in Sec. IV. First, the 3D results corresponding to a 25 Hz cw point source are presented, analyzed, and compared with other solutions. Then, the acoustic problem is solved in 4D considering the broadband source pulse. The signals received by a set of vertical arrays placed in the cross-slope direction are analyzed. Section V deals with the 3D Gaussian canyon test case. Again, results corresponding to both cw calculations and time series are presented and discussed. No reference solution is available for this test case. The received signals on two distinct vertical arrays placed along the canyon axis are then analyzed. In Sec. VI, a summary of the results of this work is provided and future improvements are suggested.

II. MATHEMATICAL MODELING

A. Fourier synthesis method

A multilayered waveguide composed of one water layer overlying one (or several) fluid sedimental layer(s) is considered. The model for each layer is three-dimensional. Cylindrical coordinates are used, where z is the depth (increasing downwards) below the ocean surface, θ is the azimuthal (bearing) angle, and r is the horizontal range, related to the Cartesian coordinates by $x = r \cos \theta$ and $y = r \sin \theta$. An isotropic, broadband point source, S , is located at $r=0$ and $z=z_S$. The acoustic wave equation,

$$\rho \nabla \cdot \left(\frac{1}{\rho} \nabla P \right) - \frac{1}{c^2} \frac{\partial^2 P}{\partial t^2} = -S(t) \frac{2\delta(z-z_S)\delta(r)}{r}, \quad (1)$$

is solved, where $P = P(r, \theta, z; t)$ is the acoustic pressure as a function of the three spatial variables r , θ , z , and time t , and $S(t)$ is the time-dependence of point source S . In Eq. (1) c and ρ represent, respectively, the varying (in space) sound speed and the density (constant within each layer). Let \hat{P} denote the Fourier transform of the time-domain acoustic pressure P , defined by

$$\hat{P}(r, \theta, z; \omega) = \int_{-\infty}^{+\infty} P(r, \theta, z; t) e^{i\omega t} dt, \quad (2)$$

where $\omega = 2\pi f$ is the angular frequency (expressed in rad/s) and f is the frequency (expressed in Hz). Then, Fourier transform of Eq. (1) leads to the frequency-domain (or Helmholtz) equation

$$\rho \nabla \cdot \left(\frac{1}{\rho} \nabla \hat{P} \right) + k_\alpha^2 \hat{P} = -\hat{S}(\omega) \frac{2\delta(z-z_S)\delta(r)}{r}, \quad (3)$$

where $k_\alpha = k(1 + i\eta\alpha)$ is the complex (to account for lossy layers) wave number, with $k = \omega/c$, α is the attenuation expressed in decibels per wavelength, $\eta = 1/(40\pi \log_{10} e)$ (with $\eta\alpha \ll 1$), and $\hat{S}(\omega)$ is the source spectrum defined by

$$\hat{S}(\omega) = \int_{-\infty}^{+\infty} S(t) e^{i\omega t} dt. \quad (4)$$

The angular frequency ω is treated as a parameter in Eq. (3). The complex-valued field $\hat{P} = \hat{P}(r, \theta, z; \omega)$ is sought as a function of the spatial variables r , θ , and z , for selected (non-negative) discrete frequencies within the frequency band of interest. The acoustic pressure \hat{P} is assumed to satisfy a pressure-release condition on the ocean surface, an outgoing radiation condition at infinity (in both range and depth), a 2π -periodicity condition in the azimuthal direction, and appropriate transmission conditions at each sedimental interface. The frequency-domain solution, \hat{P} , is then transformed to the time-domain using the following inverse Fourier transform:

$$P(r, \theta, z; t) = \frac{1}{2\pi} \int_{-\infty}^{+\infty} \hat{P}(r, \theta, z; \omega) e^{-i\omega t} d\omega, \quad (5)$$

where $\hat{P}(r, \theta, z; -\omega) = \overline{\hat{P}(r, \theta, z; \omega)}$ so that the real-valued time-domain acoustic pressure P satisfies the initial time-dependent wave equation (1). In summary, solving a pulse propagation problem with the Fourier synthesis approach^{19,20} requires one to (i) decompose the source pulse using a Fourier transform, (ii) select a frequency spacing and solve the 3D propagation problem for each discrete frequency within a frequency-band of interest, and (iii) perform inverse Fourier transforms of the frequency-domain solutions to obtain the time signal at any given receiver. As in Ref. 21, step (ii) is achieved by using a three-dimensional parabolic equation based model. Note that an alternative to the Fourier synthesis approach would be to solve the pulse propagation problem directly in the time-domain.^{19,22–26} In particular, time-domain methods related to various PE formulations can be found in Refs. 23–26.

B. Three-dimensional parabolic equation

The acoustic problem is solved in the frequency-domain using a parabolic equation (PE) approach. Dropping the source spectrum from Eq. (3) yields

$$\rho \nabla \cdot \left(\frac{1}{\rho} \nabla \hat{P}_{\text{norm}} \right) + k_\alpha^2 \hat{P}_{\text{norm}} = - \frac{2\delta(z-z_S)\delta(r)}{r}, \quad (6)$$

where the unknown is now the normalized acoustic pressure $\hat{P}_{\text{norm}}(r, \theta, z; \omega)$. Cylindrical spreading is handled by expressing $\hat{P}_{\text{norm}}(r, \theta, z; \omega)$ as

$$\hat{P}_{\text{norm}}(r, \theta, z; \omega) = H_0^{(1)}(k_0 r) \psi(r, \theta, z; \omega),$$

where $H_0^{(1)}$ denotes the zeroth-order Hankel function of the first kind and $k_0 = \omega/c_{\text{ref}}$ with c_{ref} a reference sound speed. Assuming that r^{-2} approximately commutes with $\partial/\partial r$ for $r \gg 0$, the left-hand side of Eq. (6) can be factorized, and assuming only outward propagation in range, the 3D problem based on (elliptic-type) Eq. (6) is reduced to an initial- and boundary-value problem. For any given value of ω , a complex function $\psi = \psi(r, \theta, z; \omega)$ is sought, which represents the acoustic field for $r_0 \leq r \leq r_{\text{max}}$, $0 \leq \theta \leq 2\pi$ and $0 \leq z \leq z_{\text{max}}$, and which satisfies

$$\frac{\partial \psi}{\partial r} = ik_0(\sqrt{\mathcal{I} + \mathcal{X} + \mathcal{Y}} - \mathcal{I})\psi \quad (7)$$

and $\psi(r=r_0, \theta, z; \omega) = \psi^{(0)}(\theta, z; \omega)$. Here, $\psi^{(0)}$ denotes the initial outgoing field at $r=r_0$, \mathcal{I} is the identity operator, \mathcal{X} is the 2D depth operator in the rz plane, and \mathcal{Y} is the azimuthal operator, defined as

$$\mathcal{X} = (n_\alpha^2(r, \theta, z) - 1)\mathcal{I} + \frac{\rho}{k_0^2} \frac{\partial}{\partial z} \left(\frac{1}{\rho} \frac{\partial}{\partial z} \right),$$

$$\mathcal{Y} = \frac{1}{(k_0 r)^2} \frac{\partial^2}{\partial \theta^2},$$

where $n_\alpha(r, \theta, z) = (c_{\text{ref}}/c(r, \theta, z))(1 + i\eta\alpha)$ is the complex index of refraction. In order to prevent spurious reflections from a pressure-release imposed boundary condition at z_{max} , an increasing attenuation coefficient is introduced in the lower part of the domain. The operator \mathcal{Y} handles the azimuthal diffraction term. Neglecting \mathcal{Y} in Eq. (7) but retaining azimuthal dependence in $n_\alpha(r, \theta, z)$ would lead to an $N \times 2D$ or pseudo-3D (i.e., azimuthally uncoupled) PE model which could not predict horizontal refraction. The square-root operator present in Eq. (7) is then approximated using a higher-order Padé approximation along z and a linear approximation along θ :

$$\sqrt{\mathcal{I} + \mathcal{X} + \mathcal{Y}} = \mathcal{I} + \sum_{k=1}^{n_p} \frac{a_{k,n_p} \mathcal{X}}{\mathcal{I} + b_{k,n_p} \mathcal{X}} + \frac{1}{2} \mathcal{Y} + O(\mathcal{X}^{2n_p+1}, \mathcal{Y}^2, \mathcal{X}\mathcal{Y}), \quad (8)$$

where n_p is the number of terms, and a_{k,n_p} , b_{k,n_p} , $1 \leq k \leq n_p$, are real coefficients given by²⁷

$$a_{k,n_p} = \frac{2}{2n_p + 1} \sin^2 \left(\frac{k\pi}{2n_p + 1} \right), \quad 1 \leq k \leq n_p, \quad (9)$$

$$b_{k,n_p} = \cos^2 \left(\frac{k\pi}{2n_p + 1} \right), \quad 1 \leq k \leq n_p.$$

Complex coefficients can be used to attenuate Gibb's oscillations.²⁸ The Padé series expansion is very convenient since it allows for a very-wide-angle propagation along z , the angular limitation depending on parameter n_p . It is thus able to model energy at vertical angles approaching $\pm 90^\circ$ with respect to the horizontal. The linear approximation allows only for narrow-angle propagation along θ . Substitution of

Eq. (8) into Eq. (7), and neglectation of the term in $O(\mathcal{X}^{2n_p+1}, \mathcal{Y}^2, \mathcal{X}\mathcal{Y})$ leads to

$$\frac{\partial \psi}{\partial r} = ik_0 \left(\sum_{k=1}^{n_p} \frac{a_{k,n_p} \mathcal{X}}{\mathcal{I} + b_{k,n_p} \mathcal{X}} + \frac{1}{2} \mathcal{Y} \right) \psi. \quad (10)$$

This equation accounts for refraction effects which are greater along z than along θ . It has been implemented in the research code 3DWAPE.¹³ This model has a very-wide-angle capability in depth, and a narrow-angle capability in azimuth. The original 3D PE proposed by Tappert²⁹ can be obtained by expanding the square-root in a Taylor series and retaining only the linear terms in \mathcal{X} and \mathcal{Y} ,

$$\sqrt{\mathcal{I} + \mathcal{X} + \mathcal{Y}} = \mathcal{I} + \frac{1}{2}(\mathcal{X} + \mathcal{Y}) + O(\mathcal{X}^2, \mathcal{Y}^2, \mathcal{X}\mathcal{Y}). \quad (11)$$

The resulting parabolic equation (known as the standard 3-D PE) thus has a narrow-angle capability in both depth and azimuth:

$$\frac{\partial \psi}{\partial r} = \frac{ik_0}{2} (\mathcal{X} + \mathcal{Y}) \psi. \quad (12)$$

Note that when $n_p = 1$ (which leads to the Claerbout's coefficients $a_{1,1} = 1/2$ and $b_{1,1} = 1/4$), Eq. (10) reduces to the three-dimensional parabolic equation used by Collins *et al.*¹⁰ and by Fawcett,⁸

$$\frac{\partial \psi}{\partial r} = ik_0 \left(\frac{\frac{1}{2} \mathcal{X}}{\mathcal{I} + \frac{1}{4} \mathcal{X}} + \frac{1}{2} \mathcal{Y} \right) \psi. \quad (13)$$

Since the higher-order terms neglected are in $O(\mathcal{X}^3, \mathcal{Y}^2, \mathcal{X}\mathcal{Y})$, this 3D PE has a (Claerbout) wide-angle capability in depth and a narrow-angle capability in azimuth. Instead of using a higher-order Padé approximation along z , Lee-Saad-Schultz use a Taylor series expansion along z and a linear approximation along θ :

$$\sqrt{\mathcal{I} + \mathcal{X} + \mathcal{Y}} = \mathcal{I} + \frac{1}{2} \mathcal{X} - \frac{1}{8} \mathcal{X}^2 + \frac{1}{2} \mathcal{Y} + O(\mathcal{X}^3, \mathcal{Y}^2, \mathcal{X}\mathcal{Y}). \quad (14)$$

Neglecting the higher-order terms in $O(\mathcal{X}^3, \mathcal{Y}^2, \mathcal{X}\mathcal{Y})$, the resulting equation (referred to in the literature as the LSS-3D wide angle wave equation) is

$$\frac{\partial \psi}{\partial r} = ik_0 \left(\frac{1}{2} \mathcal{X} - \frac{1}{8} \mathcal{X}^2 + \frac{1}{2} \mathcal{Y} \right) \psi. \quad (15)$$

This 3D PE has been implemented by Botseas *et al.* in the research computer code FOR3D³⁰ and applied to realistic three-dimensional environments with bottom topographic variations and sound-speed profiles.⁶

Parabolic equations can be solved numerically using various techniques. For example, Smith⁹ uses a marching algorithm based on the split-step Fourier technique in both depth and azimuth. In 3DWAPE, instead of the SSF algorithm, an alternating direction method is used. This technique is used in many 3D PE codes.^{6-8,10,18} The alternating direction method consists in splitting Eq. (10) into the following system of equations:

$$(\mathcal{I} + b_{k,n_p} \mathcal{X}) \frac{\partial \psi}{\partial r}(r, \theta, z; \omega) = ik_0 a_{k,n_p} \mathcal{X} \psi(r, \theta, z; \omega), \quad (16)$$

$$1 \leq k \leq n_p,$$

$$\frac{\partial \psi}{\partial r}(r, \theta, z; \omega) = \frac{ik_0}{2} \mathcal{Y}\psi(r, \theta, z; \omega), \quad (17)$$

and then these $n_p + 1$ equations are solved sequentially at any discrete range using an implicit Crank-Nicolson scheme. Let Δr be the increment in range. Given the 3D field ψ at discrete range value r_n , ψ is obtained at the next discrete range value $r_n + \Delta r$ in two steps. Following the notations used in Ref. 7, the first step consists in computing n_p intermediate fields denoted $u^{(1)}(\theta, z)$, $u^{(2)}(\theta, z)$, ..., $u^{(n_p)}(\theta, z)$ solving

$$\begin{aligned} & \left(\mathcal{I} + \left(b_{k,n_p} - \frac{ik_0 \Delta r}{2} a_{k,n_p} \right) \mathcal{X} \right) u^{(k)}(\theta, z) \\ &= \left(\mathcal{I} + \left(b_{k,n_p} + \frac{ik_0 \Delta r}{2} a_{k,n_p} \right) \mathcal{X} \right) u^{(k-1)}(\theta, z), \end{aligned} \quad (18)$$

for $1 \leq k \leq n_p$, where $u^{(0)}(\theta, z)$ denotes the 3D field ψ at range r_n : $u^{(0)}(\theta, z) = \psi(r_n, \theta, z; \omega)$. The second step consists in computing $\psi(r_n + \Delta r, \theta, z; \omega)$ from the last intermediate field $u^{(n_p)}(\theta, z)$ obtained in step 1, by solving

$$\begin{aligned} & \left(\mathcal{I} - \frac{ik_0 \Delta r}{4} \mathcal{Y} \right) \psi(r_n + \Delta r, \theta, z; \omega) \\ &= \left(\mathcal{I} + \frac{ik_0 \Delta r}{4} \mathcal{Y} \right) u^{(n_p)}(\theta, z). \end{aligned} \quad (19)$$

The discretization of Eq. (18) for any $1 \leq k \leq n_p$ is achieved using a piecewise-linear finite-element/Galerkin scheme. Let N and M denote the numbers of mesh points along z and θ , respectively. Solving Eq. (18) for the $N \times M$ points of the θz grid requires the inversion of n_p large algebraic linear systems of order $M \times N$. The matrix for each of the n_p systems has a block-diagonal structure. Each inversion is hence equivalent to the inversion of M (auxiliary) linear systems of order N . Since each block is a square tridiagonal matrix of order N , these inversions are performed using a fast and robust Gaussian (direct) algorithm optimized for tridiagonal matrices. The discretization of Eq. (19) is achieved using an efficient higher-order accurate finite difference (FD) scheme. The solution of Eq. (19) involves in this case the inversion of N linear systems of order M with entries in the upper right and lower left corners of the banded matrices to account for the 2π -periodicity condition along θ . The bandwidth of each block depends on the order of the centered FD formula used. Again, a fast and robust Gaussian algorithm optimized for banded matrices is used. Using a higher-order accurate FD scheme along θ allows a significant reduction of the azimuthal sampling, and faster computations (see the discussion in Ref. 13). Alternatively, Eq. (19) can also be solved using any Fourier-based transformation techniques (e.g., FFTs). The 3DWAPE code offers the possibility to use both FD- and FFT-based techniques for solving Eq. (19).

Note that all three-dimensional parabolic equations reviewed in this section make use of the following approximation:

$$\sqrt{\mathcal{I} + \mathcal{X} + \mathcal{Y}} = \sqrt{\mathcal{I} + \mathcal{X}} + \frac{1}{2} \mathcal{Y} + O(\mathcal{Y}^2, \mathcal{X}\mathcal{Y}), \quad (20)$$

and thus assume that 3D effects are sufficiently gradual (this will be discussed in the next section). They only differ in the way they approximate the term $\sqrt{\mathcal{I} + \mathcal{X}}$. In Eq. (20), the operator \mathcal{X} and the operator \mathcal{Y} are separated. Any PE model based on this formulation is thus amenable to the alternating direction method. It is worth mentioning that this approach is very advantageous for 3D modeling. Assume, for instance, that an implicit Crank-Nicolson scheme is used instead of the alternating direction method, and is applied directly on Eq. (12). Given the 3D field ψ at the discrete range r_n , ψ is obtained at the next discrete range $r_n + \Delta r$ by solving

$$\begin{aligned} & \left(\mathcal{I} - \frac{ik_0 \Delta r}{4} (\mathcal{X} + \mathcal{Y}) \right) \psi(r_n + \Delta r, \theta, z; \omega) \\ &= \left(\mathcal{I} + \frac{ik_0 \Delta r}{4} (\mathcal{X} + \mathcal{Y}) \right) \psi(r_n, \theta, z; \omega). \end{aligned} \quad (21)$$

Then, applying a FD discretization in z and θ , Eq. (21) leads to a large block-tridiagonal linear system of order $M \times N$. Unfortunately, because of its block-tridiagonal structure, this large linear system cannot be decomposed into smaller auxiliary linear systems. Furthermore, since realistic acoustic wave propagation problems generally require a large number of points in both the z and θ direction, it is not possible to use any direct algorithm (like Gaussian elimination) due to memory storage limitations. Instead, a preconditioned iterative algorithm must be used, the efficiency of the solver highly depending on the preconditioning procedure. In TRI-PARADIM, the standard narrow-angle 3D PE model was rewritten in a new coordinate system in an effort to handle properly the varying bottom topography of the three-dimensional waveguide. The resulting mathematical formulation did not allow the coordinate decomposition of the operator as for other 3D PEs. The use of the alternating direction method was thus not possible and a numerical technique similar to Eq. (21) was chosen. The reader is referred to Ref. 31 for more details on the TRIPARADIM model. Though the resulting linear systems were sparse and could be solved using an efficient preconditioning technique at each range step, it has been shown that using such an iterative algorithm could lead to prohibitive computation times in comparison with other 3D PE models that are amenable to alternating direction methods, when solving practical problems in three-dimensional environments.^{32,33} Computation time considerations are of major importance in 3D modeling, especially when broadband pulse propagation problems are addressed. In this latter case, any numerical technique using an alternating direction method should definitely be preferred to basic implicit Crank-Nicolson schemes.

C. Azimuthal wide-angle capability

The azimuthal narrow-angle capability of the 3D PE model 3DWAPE is now discussed. It is clear that the linear approximation with respect to the azimuth operator \mathcal{Y} used in Eq. (8), or more generally in Eq. (20), is only valid when $|\mathcal{Y}\psi| \ll |\mathcal{X}\psi|$. This means that any horizontal deviation should be small compared to the vertical in-plane deviation of the propagating energy. This assumption is valid for slowly varying properties. The azimuthal narrow-angle approximation

may be inappropriate for problems with large out-of-plane deviations of the outward propagating field. For such problems, one should utilize a three-dimensional parabolic equation that handles wide-angle propagation in both the z and the θ directions. Siegmann–Kriegsmann–Lee^{34,35} developed a three-dimensional parabolic equation with a wide-angle capability applying the Claerbout's coefficients to the operator $\mathcal{X} + \mathcal{Y}$:

$$\sqrt{\mathcal{I} + \mathcal{X} + \mathcal{Y}} = \mathcal{I} + \frac{\frac{1}{2}(\mathcal{X} + \mathcal{Y})}{\mathcal{I} + \frac{1}{4}(\mathcal{X} + \mathcal{Y})} + O((\mathcal{X} + \mathcal{Y})^3). \quad (22)$$

Neglecting the higher-order terms in $O((\mathcal{X} + \mathcal{Y})^3)$ then yields

$$\frac{\partial \psi}{\partial r} = ik_0 \left(\frac{\frac{1}{2}(\mathcal{X} + \mathcal{Y})}{\mathcal{I} + \frac{1}{4}(\mathcal{X} + \mathcal{Y})} \right) \psi. \quad (23)$$

The wide-angle capability of this 3D parabolic equation has been demonstrated using an asymptotic multiscale analysis.³⁵ However, it is not amenable to the use of an alternating direction method. Instead, the following numerical scheme is obtained by applying an implicit Crank–Nicolson range-stepping procedure directly on Eq. (23):

$$\left(\mathcal{I} + \left(\frac{1}{4} - \frac{ik_0 \Delta r}{4} \right) (\mathcal{X} + \mathcal{Y}) \right) \psi(r_n + \Delta r, \theta, z; \omega) = \left(\mathcal{I} + \left(\frac{1}{4} + \frac{ik_0 \Delta r}{4} \right) (\mathcal{X} + \mathcal{Y}) \right) \psi(r_n, \theta, z; \omega). \quad (24)$$

A FD technique in z and θ has been proposed and validated on several test examples.³⁶ Following our previous discussion, solving Eq. (24) may be costly. In order to take advantage of the alternating direction technique, higher-order terms may be incorporated while keeping the two operators \mathcal{X} and \mathcal{Y} separated. For instance, in PECAN,⁷ the following [1/1] Padé azimuthal expansion is used:

$$\sqrt{\mathcal{I} + \mathcal{X} + \mathcal{Y}} = \sqrt{\mathcal{I} + \mathcal{X}} + \frac{\frac{1}{2}\mathcal{Y}}{\mathcal{I} + \frac{1}{4}\mathcal{Y}} + O(\mathcal{Y}^3, \mathcal{X}\mathcal{Y}). \quad (25)$$

By neglecting higher-order terms, $O(\mathcal{Y}^3, \mathcal{X}\mathcal{Y})$, in (25), Eq. (7) then yields

$$\frac{\partial \psi}{\partial r} = ik_0 \left(\sqrt{\mathcal{I} + \mathcal{X}} + \frac{\frac{1}{2}\mathcal{Y}}{\mathcal{I} + \frac{1}{4}\mathcal{Y}} \right) \psi, \quad (26)$$

where the square-root operator present on the right-hand side is approximated using the split-step Padé algorithm.³⁷ Chen *et al.* use a quadratic Taylor series azimuthal expansion,³⁸

$$\sqrt{\mathcal{I} + \mathcal{X} + \mathcal{Y}} = \mathcal{I} + \frac{1}{2}\mathcal{X} - \frac{1}{8}\mathcal{X}^2 + \frac{1}{2}\mathcal{Y} - \frac{1}{8}\mathcal{Y}^2 + O(\mathcal{X}^3, \mathcal{X}\mathcal{Y}, \mathcal{Y}^3). \quad (27)$$

Neglecting terms in $O(\mathcal{X}^3, \mathcal{X}\mathcal{Y}, \mathcal{Y}^3)$ in Eq. (27) leads to the following parabolic equation:

$$\frac{\partial \psi}{\partial r} = ik_0 \left(\frac{1}{2}\mathcal{X} - \frac{1}{8}\mathcal{X}^2 + \frac{1}{2}\mathcal{Y} - \frac{1}{8}\mathcal{Y}^2 \right) \psi. \quad (28)$$

Equation (28) can be seen as an azimuthal quadratic correction of the *LSS-3-D Wide Angle Wave Equation* given in Eq. (15). It has been implemented in the FOR3D code. Notice that the azimuthal rational-function approximation used in Eq. (25) and the azimuthal polynomial-function approximation used in Eq. (27) are correct to quadratic terms in azimuth, but both neglect the term in $O(\mathcal{X}\mathcal{Y})$. Retaining this term would not allow the use of an alternating direction method.

In its original configuration, the 3DWAPE code had a narrow-angle capability in azimuth [see Eq. (10)]. It has been modified to handle higher-order approximations along θ while keeping the two operators \mathcal{X} and \mathcal{Y} separated. Instead of the azimuthal linear approximation in Eq. (8), a Padé series azimuthal expansion is used:

$$\sqrt{\mathcal{I} + \mathcal{X} + \mathcal{Y}} = \mathcal{I} + \sum_{k=1}^{n_p} \frac{a_{k,n_p} \mathcal{X}}{\mathcal{I} + b_{k,n_p} \mathcal{X}} + \sum_{k=1}^{m_p} \frac{a_{k,m_p} \mathcal{Y}}{\mathcal{I} + b_{k,m_p} \mathcal{Y}} + O(\mathcal{X}^{2n_p+1}, \mathcal{Y}^{2m_p+1}, \mathcal{X}\mathcal{Y}), \quad (29)$$

where m_p is the number of Padé terms and a_{k,m_p} , b_{k,m_p} , $1 \leq k \leq m_p$, are real coefficients given analytically by Eq. (9) wherein n_p is to be replaced by m_p . Then, by neglecting the last term in Eq. (29), Eq. (7) yields

$$\frac{\partial \psi}{\partial r} = ik_0 \left(\sum_{k=1}^{n_p} \frac{a_{k,n_p} \mathcal{X}}{\mathcal{I} + b_{k,n_p} \mathcal{X}} + \sum_{k=1}^{m_p} \frac{a_{k,m_p} \mathcal{Y}}{\mathcal{I} + b_{k,m_p} \mathcal{Y}} \right) \psi. \quad (30)$$

The 3D PE has now a very-wide-angle capability in depth and a very-wide-angle capability in azimuth, but, due to the term in $O(\mathcal{X}\mathcal{Y})$, the 3DWAPE model does not, strictly speaking, have a wide-angle capability. Since the depth operator \mathcal{X} and the azimuthal operator \mathcal{Y} are well separated in Eq. (30), an alternating direction method is used. Given the 3D field ψ at the discrete range r_n , ψ is obtained at the next discrete range $r_n + \Delta r$ in two steps. The first step consists in computing n_p intermediate fields denoted $u^{(1)}(\theta, z)$, $u^{(2)}(\theta, z), \dots, u^{(n_p)}(\theta, z)$ solving Eq. (18) for $1 \leq k \leq n_p$. The second step consists in computing m_p intermediate fields $v^{(1)}(\theta, z)$, $v^{(2)}(\theta, z), \dots, v^{(m_p)}(\theta, z)$ solving

$$\left(\mathcal{I} + \left(b_{k,m_p} - \frac{ik_0 \Delta r}{2} a_{k,m_p} \right) \mathcal{Y} \right) v^{(k)}(\theta, z) = \left(\mathcal{I} + \left(b_{k,m_p} + \frac{ik_0 \Delta r}{2} a_{k,m_p} \right) \mathcal{Y} \right) v^{(k-1)}(\theta, z), \quad (31)$$

for $1 \leq k \leq m_p$, where $v^{(0)}(\theta, z)$ denotes the last intermediate field $u^{(n_p)}(\theta, z)$ computed in the first step, and $v^{(m_p)}(\theta, z)$ corresponds to the 3D field ψ at the discrete range $r_n + \Delta r$: $\psi(r_n + \Delta r, \theta, z; \omega) = v^{(m_p)}(\theta, z)$. Note that for the particular value $m_p = 1$ (for which we have $a_{1,1} = 1/2$ and $b_{1,1} = 1/4$), Eq. (31) reduces to

$$\begin{aligned} & \left(\mathcal{I} + \left(\frac{1}{4} - \frac{ik_0 \Delta r}{4} \right) \mathcal{Y} \right) \psi(r_n + \Delta r, \theta, z; \omega) \\ &= \left(\mathcal{I} + \left(\frac{1}{4} + \frac{ik_0 \Delta r}{4} \right) \mathcal{Y} \right) u^{(n_p)}(\theta, z), \end{aligned} \quad (32)$$

which corresponds exactly to the equation used in PECAN to account for 3D coupling [see Eq. (2.38) of Ref. 7].

III. DESCRIPTION OF THE THREE-DIMENSIONAL TEST CASES

Two three-dimensional test cases are investigated, referred to as test cases A and B. Test case A is based on a three-dimensional extension of the original two-dimensional ASA wedge configuration and is similar to the 3D test case considered by other modelers in more recent papers.⁷⁻⁹ Test case A has been proposed as a 3D benchmark problem at the 141st ASA meeting held in Chicago in June 2001. It consists of an isovelocity water layer of sound speed $c_w = 1500$ m/s and density $\rho_w = 1$ g/cm³, overlying a lossy homogeneous half-space sedimental layer of sound speed $c_{sed} = 1700$ m/s, density $\rho_{sed} = 1.5$ g/cm³ and attenuation $\alpha_{sed} = 0.5$ dB/ λ , which leads to a critical grazing angle value of approximately 28°. There is no attenuation in the water layer. The parametrization of the water-sediment interface is given by $z_{sed}(r, \theta) = h_{sed}(x)$ where $x = r \cos \theta$ and

$$h_{sed}(x) = \begin{cases} 200(1 - x/4000) & \text{if } |x| \leq 3600 \\ 20 & \text{if } x \geq 3600 \\ 380 & \text{if } x \leq -3600. \end{cases} \quad (33)$$

The water depth decreases linearly from 200 m at $r=0$ to 20 m at $r=3.6$ km, and is range-independent for $r \geq 3.6$ km along the $\theta=0^\circ$ azimuth (up-slope direction). It increases linearly from 200 m at $r=0$ to 380 m at $r=3.6$ km, and is range-independent for $r \geq 3.6$ km along the $\theta=180^\circ$ azimuth (down-slope direction). It is invariant along the $\theta=90^\circ$ and $\theta=270^\circ$ azimuths (cross-slope directions). It thus makes an angle with a constant value of 2.86° with respect to the ocean surface at both $\theta=0^\circ$ and $\theta=180^\circ$, and leads to a zero-slope at both $\theta=90^\circ$ and $\theta=270^\circ$ (see Fig. 1).

Test case B is based on a modification of the three-dimensional gaussian canyon test case devised for the SWAM'99 Workshop¹⁷ held in Monterey CA in September 1999, and only differs from test case A in the description of the bottom topography. Test case B consists of an isovelocity water layer overlying a lossy homogeneous half-space sedimental layer (the geoacoustic parameters corresponding to each layer are identical to the ones used in test case A) with a parametrization of the water-sediment interface given by

$$h_{sed}(x) = h_0 + h_1 \exp(-x^2/\sigma^2), \quad (34)$$

where the parameters h_0 , h_1 , and σ are expressed in meters. Like test case A, the water depth only depends on the x direction. Assuming $\sigma = 4h_1$, the maximum slope of the bathymetry in the x direction (which we will refer to as the cross-canyon direction) is approximately 12.1° at $x = \sigma/\sqrt{2}$. The values $h_0 = 200$ m, $h_1 = 500$ m, and $\sigma = 4 \times h_1 = 2000$ m correspond to the ones used during the SWAM'99 workshop.

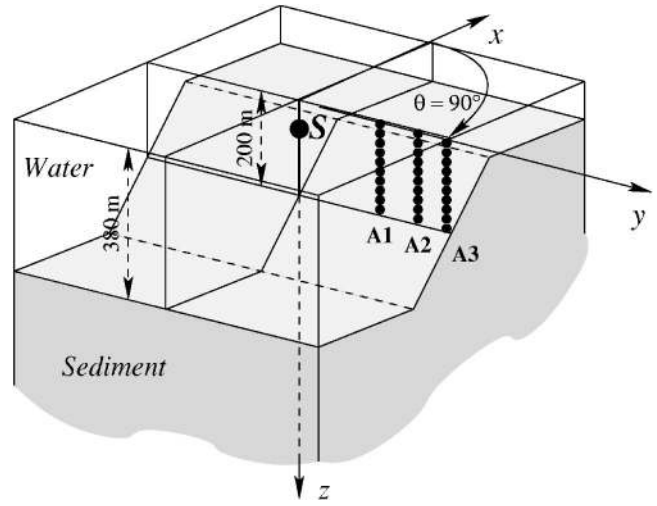


FIG. 1. Geometry of the 3D (truncated) wedge shaped waveguide considered in test case A.

In this paper, $h_0 = 20$ m, $h_1 = 180$ m, and $\sigma = 4h_1 = 720$ m. The configuration used in test case B is depicted in Fig. 2. The water depth decreases from 200 m at $r=0$ to 20 m at $r \rightarrow \infty$ along the $\theta=0^\circ$ and $\theta=180^\circ$ azimuths (cross-canyon directions). It is invariant along the $\theta=90^\circ$ and $\theta=270^\circ$ azimuths (along-canyon directions). It makes a varying angle with respect to the ocean surface (with a maximum value of approximately 12.1° at $r=509.12$ m) at $\theta=0^\circ$ and $\theta=180^\circ$, and leads to a zero-slope at $\theta=90^\circ$ and $\theta=270^\circ$.

For both test cases, an isotropic point source is located at point $S = (x_S = 0, y_S = 0, z_S = 40$ m). Its time dependence is a Hanning-weighted four-period sine wave (see Fig. 3) given by

$$S(t) = \begin{cases} \frac{1}{2} (1 - \cos(\omega_c t/4)) \sin(\omega_c t) & \text{if } 0 \leq t \leq 4/f_c \\ 0 & \text{if } t > 4/f_c, \end{cases} \quad (35)$$

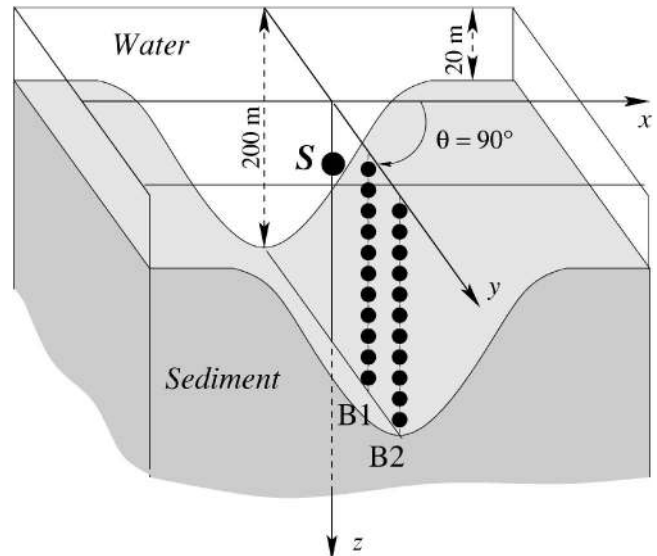


FIG. 2. Geometry of the 3D Gaussian canyon waveguide considered in test case B.

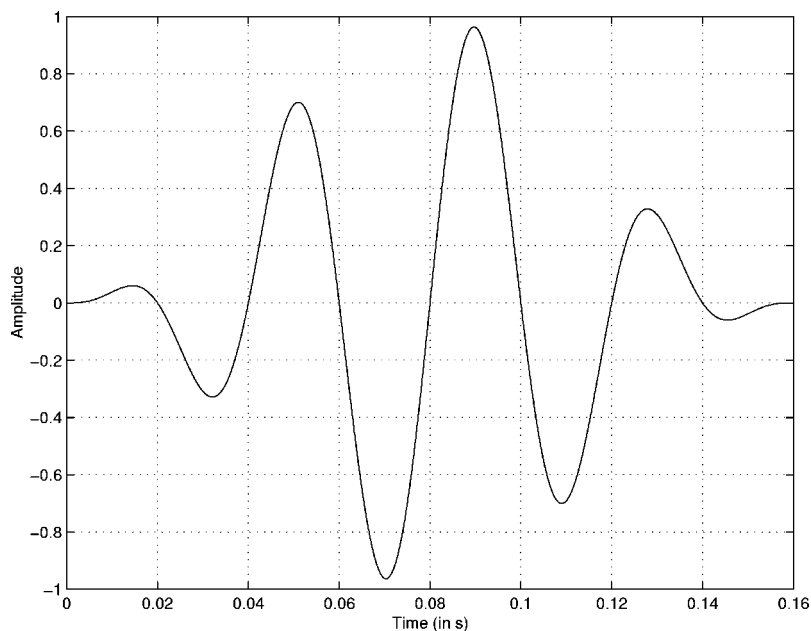


FIG. 3. Time-dependence of the source pulse, for test cases A and B.

where $\omega_c = 2\pi f_c$ and $f_c = 25$ Hz. The source pulse is centered at frequency $f_c = 25$ Hz with a 40 Hz bandwidth covering the band 5–45 Hz. The amplitudes of both the real and imaginary parts of the source spectrum are very small for frequencies below 5 Hz and above 45 Hz (see Fig. 4). The pulse length is 0.16 s. For both test cases, the geometry of the waveguide at $\theta = 90^\circ$ (which corresponds to the cross-slope direction for test case A and to the canyon axis for test case B) is characterized by a zero-slope (the water depth is constant and equal to 200 m). Due to the geometry of the two waveguides, large 3D effects are expected in this direction, along which several vertical arrays are placed. In test case A, three vertical arrays labeled A1, A2, and A3 are placed across slope at ranges $r_{A1} = 16$ km, $r_{A2} = 22$ km, and $r_{A3} = 25$ km from the source S . In test case B, two vertical arrays labeled B1 and B2 are placed along the canyon axis at ranges r_{B1}

$= 16$ km and $r_{B2} = 20$ km from the source S . Each of the vertical arrays is composed of 19 elements evenly spaced in depth between 10 and 190 m. Note that, for both test cases, the vertical arrays and the source lie in the same 200 m isobath vertical plane. All the numerical simulations shown in the next sections were performed on a 2.2 GHz mono-processor Dell-workstation. Neither vectorization nor parallel computing was used. Unless specified otherwise, all the following numerical results were obtained using the 3D PE model 3DWAPE.

IV. RESULTS FOR THE 3D ASA WEDGE

A. cw point source results

Since the source pulse is centered at $f_c = 25$ Hz, the acoustic problem at that specific frequency is treated first.

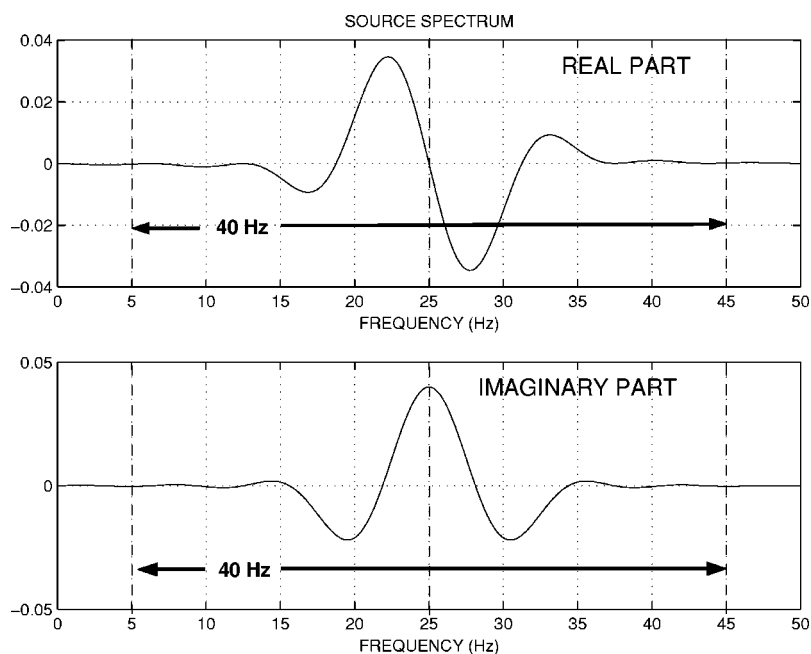


FIG. 4. Spectrum of the source pulse, for test cases A and B.

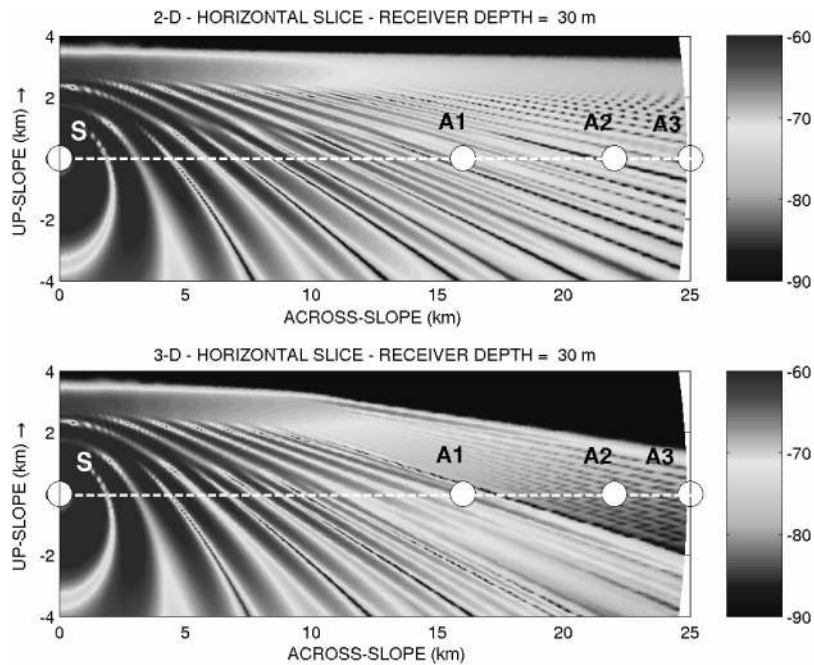


FIG. 5. Transmission loss (in dB re 1 m) at 25 Hz at a depth of 30 m for test case A corresponding to $N \times 2D$ (upper subplot) and 3D (lower subplot) PE calculations. For both calculations, a modal sum was used as a starting field. The 200 m isobath is indicated by a dashed white line.

The $N \times 2D$ and 3D computations were carried out using $\Delta r = 10$ m, $\Delta z = 1$ m (i.e., $\Delta r = \lambda/6$ and $\Delta z = \lambda/60$ where λ denotes the acoustic wavelength) and $n_p = 2$. The maximum computation range is $r_{\max} = 25$ km and the reference sound speed is $c_{\text{ref}} = 1500$ m/s. The $N \times 2D$ and 3D PE algorithms were initialized at $r = 0$ using a modal source. Since long-range propagation is considered, the modal sum was limited to the discrete modal spectrum. Only three propagating modes are present at a frequency of 25 Hz at the source location. The maximum depth of the computational grid is $z_{\max} = 600$ m. An increasing attenuation coefficient $\alpha_{\text{abs}}(z)$ was introduced in the lower part of the domain (corresponding to depths between $z_{\text{abs}} = 450$ m and $z_{\max} = 600$ m) to prevent spurious reflections from the pressure-release imposed boundary condition at z_{\max} . For the 3D calculations, a Padé 1 approximation in azimuth (i.e., $m_p = 1$) and an eighth-order FD azimuthal scheme with $M = 3240$ points (i.e., an azimuthal step size of $1/9$ th of a degree) were used. This azimuthal increment corresponds to an arclength increment ΔS of the order of $3\lambda/4$ at the maximum computation range r_{\max} . As shown in Ref. 32, using a second-order FD azimuthal scheme would require in this case $M = 23\,040$ discrete points in azimuth, i.e., an azimuthal step size of $1/64$ th of a degree (this azimuthal increment corresponding to an arclength increment ΔS of the order of $\lambda/10$ at the maximum computation range r_{\max}).

Gray-scale images of the transmission loss (TL) $= -20 \log_{10}(|\psi(r, \theta, z; \omega_c)|/\sqrt{r})$ with $\omega_c = 2\pi f_c$ at a receiver depth of 30 m corresponding to $N \times 2D$ and 3D calculations are displayed in Fig. 5. The $\theta = 90^\circ$ direction corresponding to the 200 m isobath is indicated by a dashed line. The positions of the source S and the three vertical arrays $A1$, $A2$, $A3$ are also indicated on each subplot. Due to the geometrical symmetry of the problem about the up-slope direction, both $N \times 2D$ and 3D solutions are displayed as a function of range and azimuth in a limited azimuthal sector.

Figure 6 shows transmission loss-vs-range curves at $z = 30$ m and $\theta = 90^\circ$ (across-slope). The thin dashed curve is a $N \times 2D$ PE calculation and the bold solid curve is a 3D PE calculation. Comparing the two subplots of Fig. 5, the effects of azimuthal coupling are evident, mainly in the vicinity of the cross-slope direction and at long ranges. These effects are well known and have been explained in detail by several authors. They correspond to intramodal interference effects. Recall that three propagating modes are excited at the source. Since the vertical geometry in the cross-slope direction (characterized by a zero-slope) is a classical 200-m-deep Pekeris waveguide, any 2D or $N \times 2D$ model can predict the presence of the three initial modes at $\theta = 90^\circ$ for $0 \leq r$

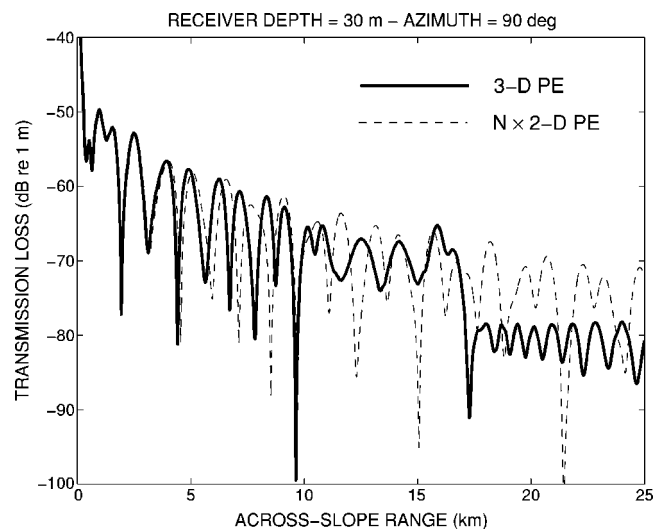


FIG. 6. $N \times 2D$ and 3D transmission loss (in dB re 1 m) comparisons at 25 Hz at a receiver depth of 30 m along a 200 m isobath in the cross-slope direction for test case A. The thin dashed curve is an $N \times 2D$ PE calculation and the bold solid curve is a 3D PE calculation. For both calculations the Greene's source was used as a starting field.

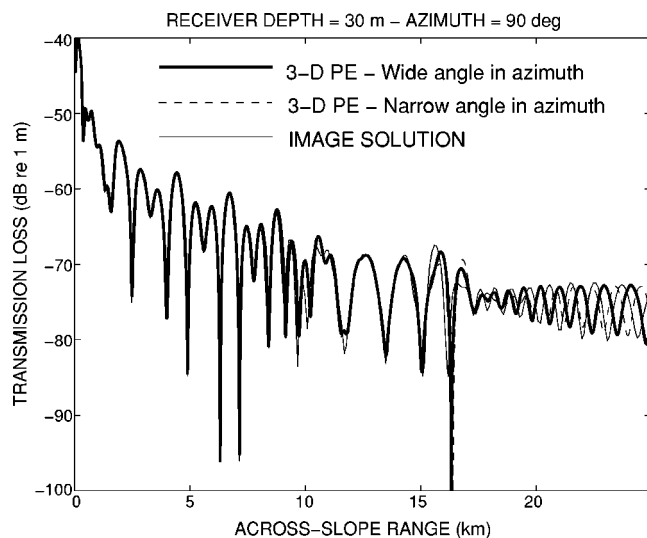


FIG. 7. 3D transmission loss (in dB re 1 m) comparisons at 25 Hz at a receiver depth of 30 m along a 200 m isobath in the cross-slope direction for test case A. The thin solid curve corresponds to the image solution. The two other curves are 3D PE calculations using a wide-angle (bold solid curve) or a narrow-angle (thin dashed curve) approximation in azimuth. The source depth is 100 m. Both 3D PE calculations were initialized using the Greene's source.

≤ 25 km. The use of a full 3-D PE (i.e., azimuthally coupled model) causes these three propagating modes to be horizontally refracted down the slope, which leads to a succession of three distinct zones in the cross-slope direction (see Fig. 6). For ranges less than approximately 11 km, the three initial propagating modes are present. Only two modes are present for $r \geq 11$ km up to $r \approx 16$ km, due to the 3D shadowing effect of mode 3. After $r \approx 16$ km where the mode shadowing effect of mode 2 occurs, only mode 1 is present. The interference pattern in the 3D solution starting at $r \approx 17.5$ km corresponds to the 3D mode self-interference effect of mode 1.

To show that no significant 3D effects are omitted in the 3D PE calculations, the results were compared with a reference solution based on the image source method and originally provided by Westwood.³⁹ This analytical solution is expressed as a sum of ray fields, each of which take the form of a double integral over plane waves. Details of the method are given in Ref. 16. Note that the source depth was 100 m to match the original ASA benchmark problem. The 3D PE and the image solutions are plotted in Fig. 7. The bold solid curve is the 3D PE solution obtained using two Padé terms in depth ($n_p = 2$) and one Padé term in azimuth ($m_p = 1$). Also plotted on the same figure as a thin dashed curve is the 3D PE solution obtained using two Padé terms in depth and a narrow-angle azimuthal approximation. The 3D PE calculations were initialized using the Greene's source.⁴⁰ We observe an overall good agreement between the two 3D PE solutions and the image solution in the cross-slope direction, showing that both models predict the same 3D effects. However, there are some differences, notably a shift in the phasing at long ranges mainly where mode 1 interferences occur. Note that the 3D PE solution obtained using a Padé 1 approximation in azimuth is closer to the reference solution than the azimuthal narrow-angle 3D PE solution, although a phase shift is still present. The use of higher-order approxi-

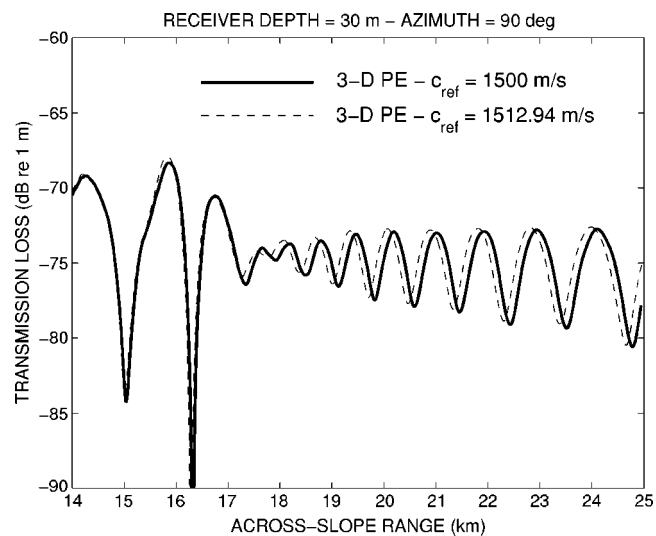


FIG. 8. 3D transmission loss (in dB re 1 m) comparisons at 25 Hz at a receiver depth of 30 m along a 200 m isobath in the cross-slope direction ($\theta = 90^\circ$, $14 \text{ km} \leq r \leq 25 \text{ km}$) for test case A. The bold solid curve is a 3D PE calculation with $c_{\text{ref}} = 1500 \text{ m/s}$ (same solution as shown in Fig. 7) and thin dashed curve is a 3D PE calculation with $c_{\text{ref}} = 1512.94 \text{ m/s}$. The source depth is 100 m. The Greene's source was used as a starting field.

mations in azimuth (i.e., increasing the number m_p of Padé terms) does not improve phase predictions. Recall that the PE solutions depend on the value of the reference sound speed c_{ref} . For the solutions shown in Fig. 7, $c_{\text{ref}} = 1500 \text{ m/s}$. Figure 8 shows 3D PE solutions obtained using two distinct values of c_{ref} . The bold solid curve corresponds to $c_{\text{ref}} = 1500 \text{ m/s}$ (the value of the sound speed in the homogeneous water layer) and the thin dashed curve to $c_{\text{ref}} = 1512.94 \text{ m/s}$ (the value of the horizontal phase speed of mode 1 at the source location). As already pointed out by Smith,⁹ changing the reference sound speed value induces a shift in the PE solutions. This shift is yet less pronounced than that between PE solutions shown in Fig. 7. This suggests that the disagreement between the image and the PE results is mainly due to the fact that the 3D PE model does not have a wide-angle capability since the term in $O(\lambda \mathcal{Y})$ is not handled (see the discussion in Sec. II C). However, despite the mismatch in the mode 1 interference pattern, all the physical 3D effects are reproduced by the 3D PE model.

B. Modal initialization results

Azimuthal coupling effects may be easily observed by exciting individual modes at the source location and propagating them outward in range. The 3D PE marching algorithm was initialized by each of the three propagating modes separately. Figure 9 shows TL plots (horizontal slices at constant depth $z = 30 \text{ m}$) obtained by initializing the 3D PE model using mode 1, mode 2, and mode 3. In order to reduce the phase error in PE calculations, the horizontal modal phase speed was used for the reference sound speed, i.e., $c_{\text{ref}} = 1512.94 \text{ m/s}$ for mode 1, $c_{\text{ref}} = 1554.44 \text{ m/s}$ for mode 2, and $c_{\text{ref}} = 1632.42 \text{ m/s}$ for mode 3. For each mode, the source field was assumed to be omnidirectional. Vertical cross sections of the 3D PE solutions for mode 1, mode 2, mode 3

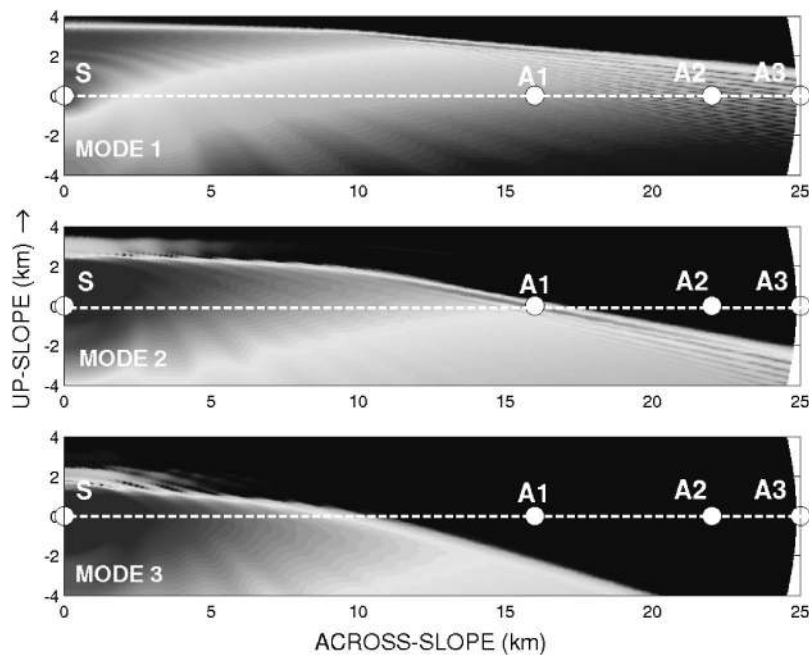


FIG. 9. Transmission loss (in dB re 1 m) at 25 Hz at a depth of 30 m for test case A corresponding to 3D PE calculations and different omnidirectional mode excitations. From top to bottom: mode 1, mode 2, and mode 3. On each subplot, the 200 m isobath is indicated by a dashed line.

along the $\theta=90^\circ$ direction are shown in Fig. 10. Also shown in Fig. 10 is the 3D PE solution obtained initializing by the Greene's source.

The 3D PE results were compared with the predictions from adiabatic modal theory.⁴¹ Figure 11 shows the modal ray diagrams in the (horizontal) yx plane for each omnidirectional modal initialization. The modal ray paths were calculated using the method given in Ref. 8. Hereafter, a modal-ray path that corresponds to the m th mode and makes initially an angle ϕ_0 with the y axis (i.e., $\phi_0=0^\circ$ points across slope) is denoted Γ_{m,ϕ_0} (see Fig. 12). According to the Cartesian coordinate system chosen, for any value of m

$\in \{1,2,3\}$ and any value of $\phi_0 \in]-90^\circ, 90^\circ[$, the modal-ray path Γ_{m,ϕ_0} is a representative function $y \mapsto x_{m,\phi_0}(y)$ satisfying the following Cauchy problem

$$\frac{dx}{dy} = \frac{\sqrt{1 - (c_m(x) \times \cos(\phi_0)/c_{r,m})^2}}{c_m(x) \times \cos(\phi_0)/c_{r,m}}, \quad y \geq 0, \\ x(y=0) = 0. \quad (36)$$

Here, $\phi_0=90^\circ$ ($\phi_0=-90^\circ$) corresponds to an initial launch in the up-slope direction (in the down-slope direction) and c_m is the x -dependent phase velocity of the m th mode satisfying $c_w < c_m(x) < c_{sed}$ and $c_m(x=0) = c_{r,m}$, where $c_{r,m}$ is

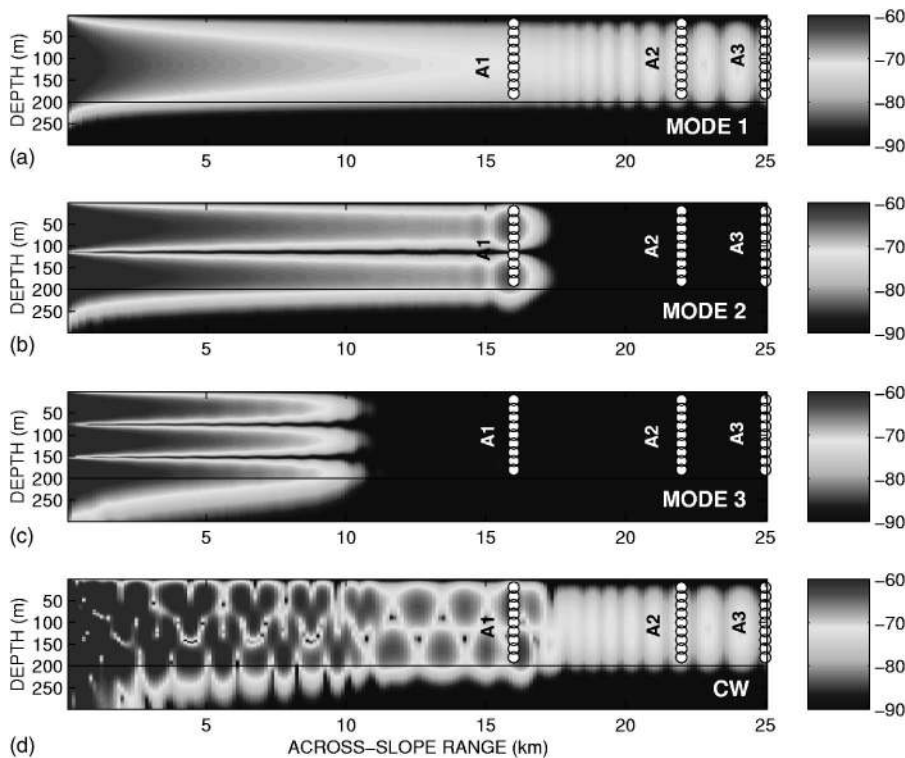


FIG. 10. 3D transmission loss (in dB re 1 m) at 25 Hz for test case A (vertical slices in the cross-slope direction) corresponding to 3D PE calculations and (a) mode 1, (b) mode 2, (c) mode 3, and (d) Greene's source excitations.

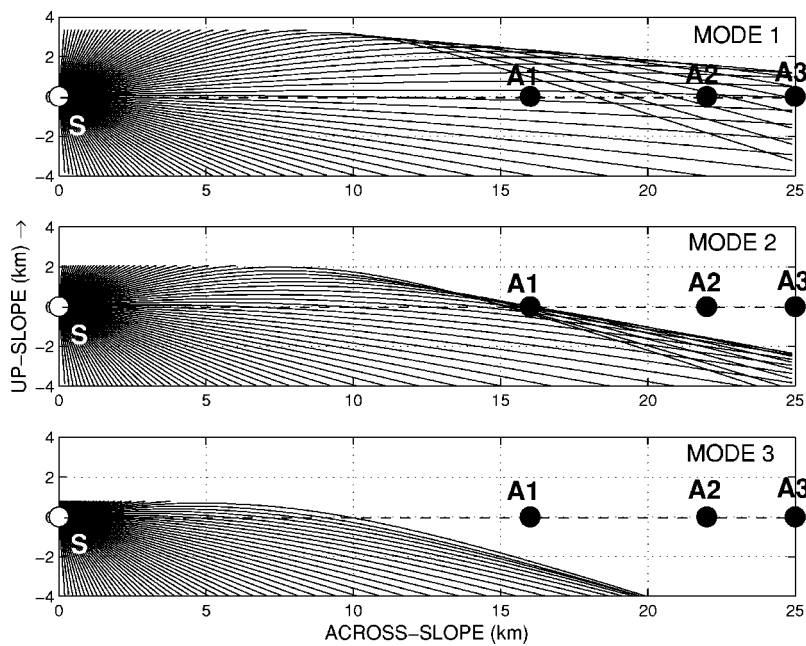


FIG. 11. Modal ray diagrams (top view) for test case A, obtained solving the differential equation given in (36) for $-90^\circ < \phi_0 < 90^\circ$. From top to bottom: mode 1, mode 2, and mode 3.

the horizontal phase speed of the m th mode at the source location. The value of $c_m(x)$ for any given x is numerically evaluated by solving

$$\tan(\sqrt{(\omega_c/c_w)^2 - (\omega_c/c_m(x))^2} \times h_{\text{sed}}(x)) = -\frac{\rho_{\text{sed}}}{\rho_w} \times \frac{\sqrt{(\omega_c/c_w)^2 - (\omega_c/c_m(x))^2}}{\sqrt{(\omega_c/c_m(x))^2 - (\omega_c/c_{\text{sed}})^2}},$$

where $\omega_c = 2\pi f_c$. Note that a modal ray is stopped if it reaches an x coordinate such that $c_m(x)$ does not belong to $]c_w, c_{\text{sed}}[$ (i.e., when mode m becomes leaky). Characteristics of the modal rays that connect the source S with one of the three arrays A1, A2, and A3, are listed in Table I.

Comparison of the results displayed in Figs. 9 and 11 shows that the 3D PE solutions are in good agreement with the predictions from adiabatic modal theory. A modal ray which has an initial launch direction ϕ_0 toward the wedge apex turns around, as long as its grazing angle does not exceed the critical angle. A region of multiple arrivals is created in the vicinity of the cross-slope direction for sufficiently large ranges from the source, followed by a shadow region. Due to the increasing grazing angle with respect to the mode number, 3D effects are stronger for higher modes

than for lower modes. No shadow zone is observed for mode 1 for $r \leq 25$ km in the cross-slope direction. Computations for ranges greater than 25 km for mode 1 would also show a shadow zone in the cross-slope direction. Following Glegg *et al.*,² three regions exist in the wedge-shaped waveguide for each modal initialization: (1) an inner region (corresponding to ϕ_0 greater than a critical launch angle ϕ_{crit}) where the modal rays propagating upslope exceed the critical grazing angle and are not turned around; (2) an outer region (corresponding to ϕ_0 less than ϕ_{crit}) where the modal-ray-turn-around occurs; and (3) a shadow region where there is no propagation. The value of the critical launch angle ϕ_{crit} depends on the mode number: $\phi_{\text{crit}} \approx 27^\circ$ for mode 1, $\phi_{\text{crit}} \approx 23.7^\circ$ for mode 2, and $\phi_{\text{crit}} \approx 16^\circ$ for mode 3.

Results obtained with both models (PE and adiabatic mode) confirm the presence of mode 1 at the three vertical arrays A1, A2, and A3. Note that arrays A2 and A3 (unlike array A1) both lie in the multiple mode arrival area of mode 1, which means that multiple modal ray path arrivals exist for mode 1 on array A2 and array A3 (see Table I). Indeed, there are two modal ray path arrivals for mode 1 on array A2 (on array A3), the first one with a shallow angle ϕ_0

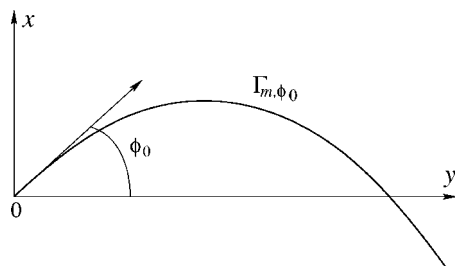


FIG. 12. Schematic of a modal-ray path Γ_{m,ϕ_0} in the (horizontal) yx plane corresponding to mode m , with initial launch angle ϕ_0 . The y axis (the x axis) corresponds to the cross-slope (up-slope) direction in the wedge shaped waveguide considered in test case A. The source is placed at $x=y=0$.

TABLE I. Characteristics (for a 25 Hz cw point source, test case A) of the modal rays launched from the source S and connected with one of the three arrays A1, A2, A3. The angle ϕ_0 denotes the initial launch angle ($\phi_0 = 0^\circ$ points across-slope) of the modal eigenray, and L_{m,ϕ_0} denotes the length of the modal eigenray path Γ_{m,ϕ_0} .

Array	Mode m	ϕ_0 (deg)	L_{m,ϕ_0} (m)
A1	1	+1.8	16 002
A1	2	+13.5	16 186
A1	2	+16.5	16 300
A2	1	+2.7	22 008
A2	1	+19.7	22 845
A3	1	+3.2	25 013
A3	1	+16.7	25 640

$= +2.7^\circ$ ($\phi_0 = +3.2^\circ$) with respect to the cross-slope direction, and the second one with a steeper angle $\phi_0 = +19.7^\circ$ ($\phi_0 = +16.7^\circ$). Two distinct time arrivals of the signal carried by mode 1 on both arrays A2 and A3 are thus expected, but only one single time arrival of the signal carried by mode 1 on array A1. The array A1 lies in the limit of the insonified region of mode 2. The signal carried by mode 2 should be present at array A1 only. In addition, the array A1 lies in the multiple mode arrival area of mode 2. Two distinct modal ray path arrivals for mode 2 with initial launch angles $\phi_0 = +13.5^\circ$ and $\phi_0 = +16.5^\circ$ are detected on array A1. Hence, two distinct arrival times of the signal carried by mode 2 on A1 are expected. Obviously, the three arrays A1, A2, and A3 lie in the shadow zone region of mode 3. No arrival of the signal carried by mode 3 is thus detected by any of the three arrays.

C. Broadband results

The case of the broadband source signal given in Eq. (35) is now discussed. The pulse response at a specific receiver R of range r_R , azimuth θ_R , and depth z_R , is obtained via a Fourier transform of the frequency-domain solution using

$$P(r_R, \theta_R, z_R; t) = \frac{1}{2\pi} \int_{-\infty}^{+\infty} \hat{S}(\omega) \hat{P}_{\text{norm}}(r_R, \theta_R, z_R; \omega) e^{-i\omega t} d\omega, \quad (37)$$

where $\hat{S}(\omega)$ is the source spectrum given by Eq. (4), and \hat{P}_{norm} is the solution of the normalized frequency-domain wave equation (6). In Eq. (37), \hat{P}_{norm} is set to zero for any (non-negative) frequency f outside the band 5–45 Hz. The frequency integral in Eq. (37) is evaluated numerically using a discrete Fourier transform (DFT). A time window of length $T = 7$ s, with 4096 points, is used in the DFT algorithm. This yields values of the received signal at R in the time window $[t_{\min}, t_{\min} + T]$ with a very fine time resolution Δt of 0.0017 s ($\Delta t = T/4096$). The length of the time window corresponds to a frequency sampling Δf of 0.1429 Hz ($\Delta f = 1/T$), which leads to 281 discrete values within the frequency-band 5–45 Hz. Producing a pulse response at receiver R requires first computing values of \hat{P}_{norm} at 281 discrete frequencies. This is achieved through repeated solution of the 3D PE model for uniformly distributed discrete frequencies ranging from 5 to 45 Hz and for $0 \leq r \leq r_R$, $0 \leq \theta \leq 2\pi$, $0 \leq z \leq z_{\max}$.

For each solution at a single frequency f , several parameters need to be changed, their values depending on the value of the frequency f , or equivalently, of the acoustic wavelength λ . Suitable selections of the range, azimuthal, and depth increments Δr , $\Delta \theta$, Δz are crucial. For instance, undersampling (oversampling) the azimuthal direction may appear inappropriate to accurately compute the 3D effects (may lead to untimely computations). It is well established that the range and depth increments Δr and Δz should be sufficiently small in comparison to the acoustic wavelength λ . Our calculations were carried out using $\Delta r = \lambda/6$ and $\Delta z = \lambda/60$. Since an eighth-order FD scheme was used in azimuth, selection of the azimuthal increment $\Delta \theta = 2\pi/M$ was achieved

using a less restricting criterion with respect to the acoustic wavelength: $\Delta \theta$ (or equivalently M) was selected such that $\Delta S \approx 3\lambda/4$, where ΔS denotes the arclength increment at the maximum computation range r_{\max} . Note that using a second-order FD scheme in azimuth would require that $\Delta S \approx \lambda/10$. Our calculations were carried out using $M = 648$ at $f = 5$ Hz and $M = 5832$ at $f = 45$ Hz. For intermediate values of the frequency within the band 5–45 Hz, the number of discrete points in azimuth is obtained by linearly interpolating between 648 and 5832. For each frequency-domain calculation, the 3D PE marching algorithm was initialized at $r = 0$ using the Greene's source. Two Padé terms in depth (i.e., $n_p = 2$) and one Padé terms in azimuth (i.e., $m_p = 1$) were used. The maximum depth z_{\max} of the computation grid was placed several wave-lengths below the maximum depth of the sea-floor and a layer of increasing absorption was placed in the lower part of the domain (just above z_{\max}) to attenuate the reflected energy, its width also depending on the acoustic wavelength.

The signal arrivals on the three vertical arrays A1, A2, and A3 were calculated. Comparisons of the signals received on vertical array A1 at a depth of 20 m corresponding to 2D and 3D computations are shown in Fig. 13. Both 2D and 3D solutions were multiplied by a factor $r_{A1} = 16\,000$ m to compensate for spherical spreading. The pulse responses on vertical arrays A1, A2, and A3 were calculated using $t_{\min} = 10.6$ s, $t_{\min} = 14.6$ s, $t_{\min} = 16.6$ s, respectively. They are displayed in Figs. 14, 15, and 16. The received signals are plotted intentionally as stacked time series versus depth which is helpful when analyzing the modal structure of the signal arrivals. Snapshots of the propagating pulse in the cross-slope direction at two distinct times, $t = 10.7$ s and $t = 16.7$ s, are shown in Figs. 17 and 18, respectively. For comparison, the signals obtained using 2D calculations are also shown.

Let us analyze first the signal arrivals on receiver arrays A1, A2, and A3, computed using a 2D PE model. The geometry of the waveguide in the cross-slope direction (characterized by a zero-slope) is seen by the 2D PE model as a classical 200-m-deep waveguide, which leads to the existence of three propagating modes when a 25 Hz cw source signal is considered. As expected, considering a broadband source pulse with a central frequency of 25 Hz, the propagating signal splits up in three distinct wave packets, which correspond to the signal carried by the three propagating modes of the waveguide. Now, using a 3D PE model, the signal arrivals exhibit only two distinct mode arrivals (instead of three as predicted by 2D calculations) at each of the three vertical arrays A1, A2, and A3. For each of them, it is clear that the first wave packet corresponds to the signal carried by mode 1. Indeed, its amplitude is low near the ocean surface, increases with depth toward mid-depth, then decreases toward $z = 200$ m. This is obviously the depth dependence of mode 1. Following the same analysis, the second wave packet received on A1 (respectively, on A2 and A3) corresponds to the signal carried by mode 2 (respectively, by mode 1). These observations are coherent with the predictions of the previous section. Indeed, as expected, the signal carried by mode 1 is present for each of the three vertical arrays A1, A2, and

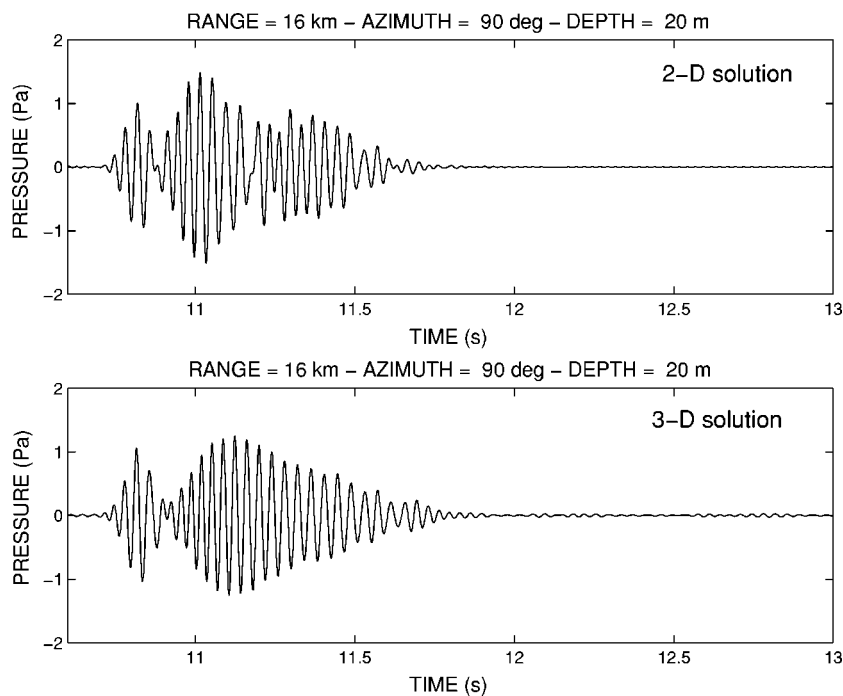


FIG. 13. Comparison of broadband pulse solutions for test case A and array A1 at a depth of 20 m: (upper) 2D calculation and (lower) 3D calculation.

A3. Since only A2 and A3 lie in the multiple mode arrival area of mode 1, two distinct mode 1 arrivals are observed on A2 and A3 (and only one single mode 1 arrival on A1), the first one corresponding to a modal ray path with a shallow angle with respect to the cross-slope direction, and the second one (weaker) to a modal ray path with a steeper angle. The time delay between the first and second time arrival of mode 1 is shorter at A3 than at A2. As expected, the signal carried by mode 2 is only present at A1 (recall that A1 lies in the limit of the insonified region of mode 2). Note that the second wave packet received on A1 corresponds to the

merger of the two distinct (but close) time arrivals of mode 2. It thus appears more dispersed in time than the single mode 2 arrival predicted by a 2D calculation. Since the three arrays A1, A2, and A3 all lie in the shadow zone region of mode 3, no mode 3 signal arrival is observed at A1, A2, and A3. Note that all the modal eigenrays have been constantly refracted in the horizontal direction during their upslope and downslope propagation. Thus, the corresponding wave packets are different from the wave packets predicted using a 2D model.

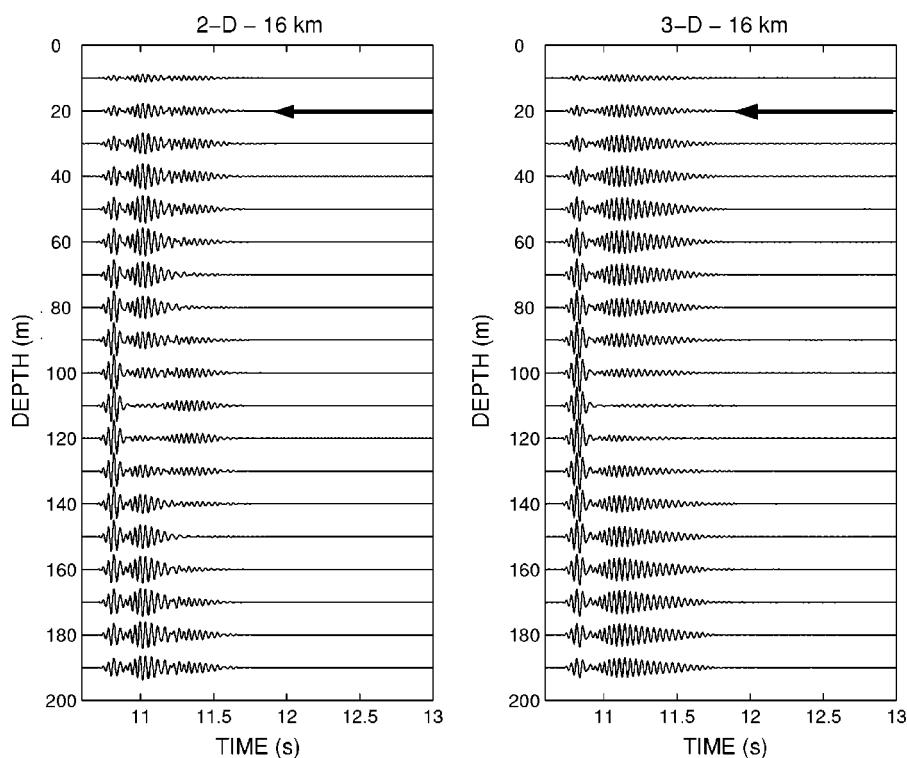


FIG. 14. Stacked time series vs depth for test case A corresponding to vertical array A1: (left) 2D calculation and (right) 3D calculation.

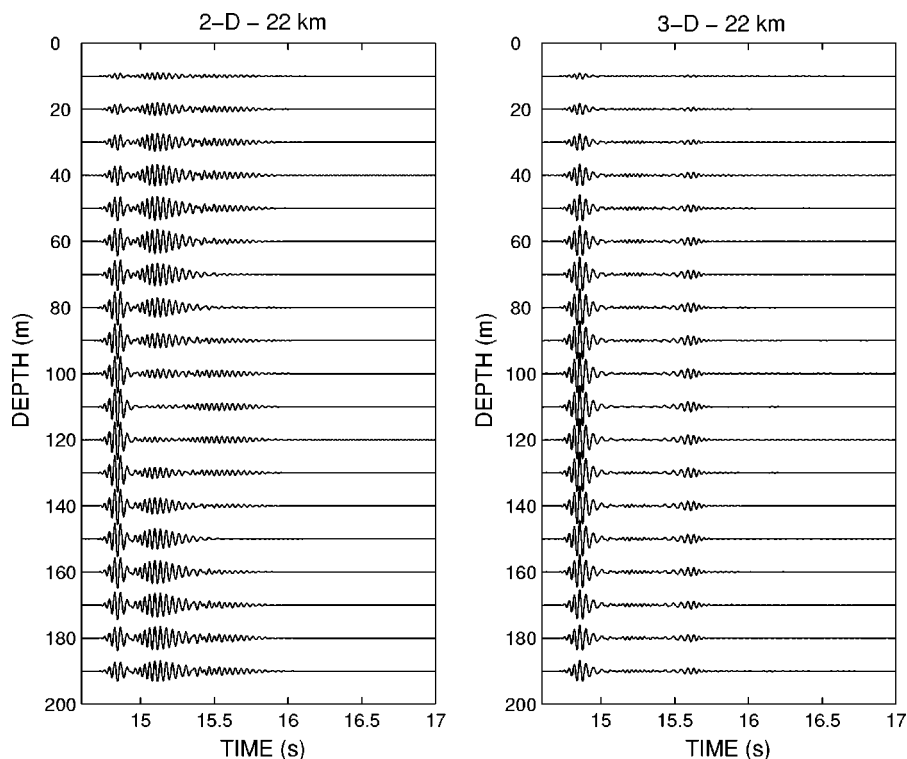


FIG. 15. Stacked time series vs depth for test case A corresponding to vertical array A2: (left) 2D calculation and (right) 3D calculation.

V. RESULTS FOR THE 3D GAUSSIAN CANYON

A. cw point source results

The acoustic problem involving a 25 Hz cw point source is analyzed first. The $N \times 2D$ and 3D results presented hereafter were obtained using the same range and depth increments as in test case A ($\Delta r = 10$ m, $\Delta z = 1$ m). Both $N \times 2D$ and 3D calculations were generated using a fifth-order Padé 3 approximation in depth (i.e., $n_p = 3$). For the 3D cal-

culations, a third-order Padé 1 approximation in azimuth (i.e., $m_p = 1$) and $M = 2880$ points were used. The number of discrete points used in azimuth is less than in test case A simply because the value of the maximum computation range r_{\max} has been reduced from 25 to 20 km. As in test case A, the azimuthal increment $\Delta\theta = 2\pi/2880$ corresponds to an arclength increment ΔS of the order of $3\lambda/4$ at the maximum computation range $r_{\max} = 20$ km.

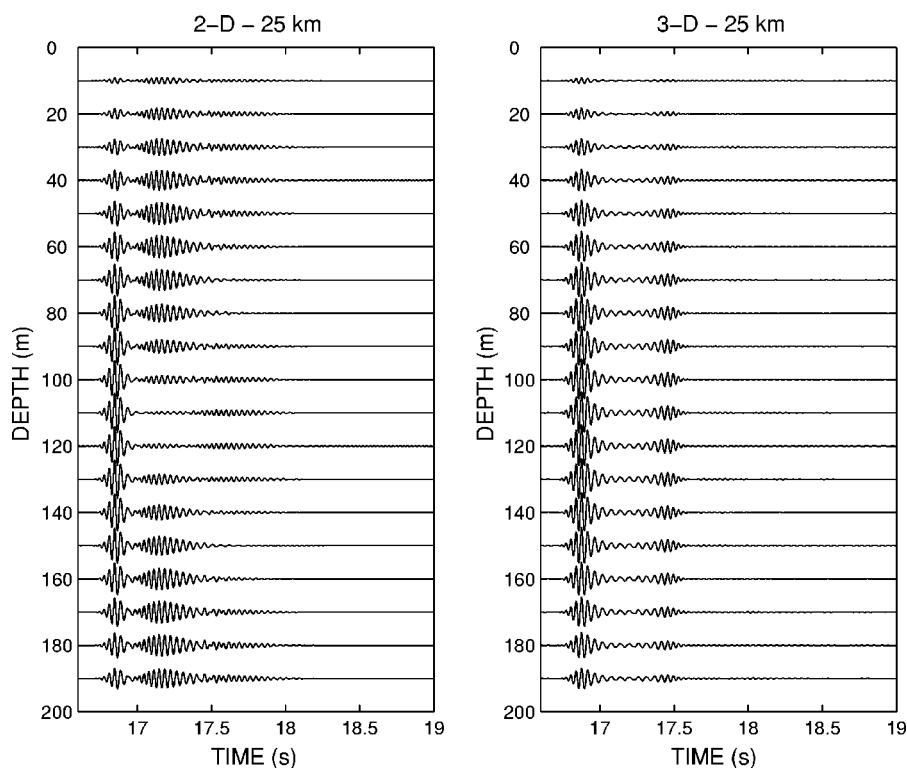


FIG. 16. Stacked time series vs depth for test case A corresponding to vertical array A3: (left) 2D calculation and (right) 3D calculation.

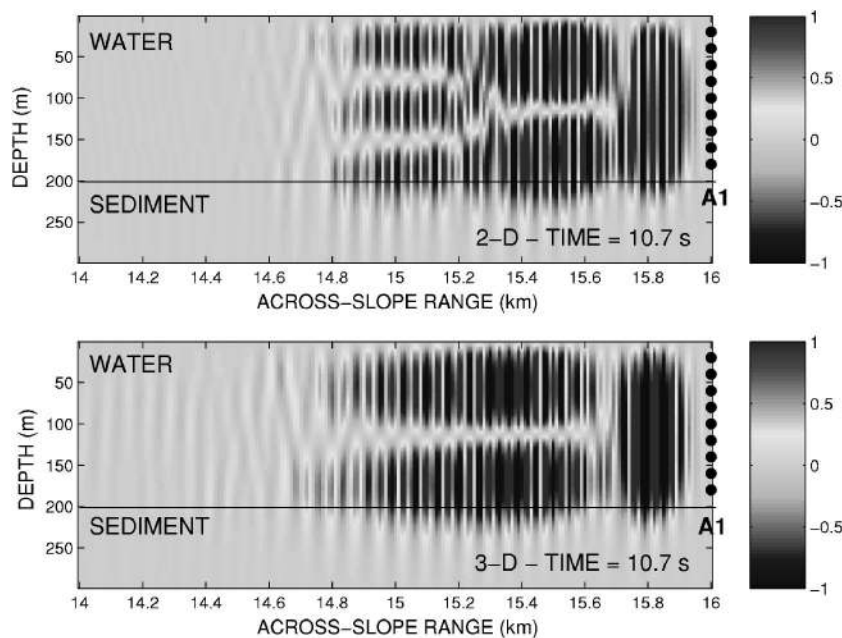


FIG. 17. Snapshots of the propagating pulse for test case A at $t = 10.7$ s: (upper) 2D calculation and (lower) 3D calculation.

Gray-scale images of the transmission loss (horizontal slices at a receiver depth of 30 m) corresponding to $N \times 2D$ and 3D calculations are shown in Fig. 19. For both of them, the modal sum was used as a starting field. A maximum computation depth of 600 m and a reference sound speed of 1500 m/s were used. The $\theta = 90^\circ$ direction corresponding to the canyon axis is indicated by a dashed line. The positions of the source S and the two vertical arrays B1, B2 are also indicated on each subplot. Like test case A, due to the geometrical symmetry of the problem about the x axis, both solutions are displayed as a function of range and azimuth in a limited azimuthal sector. By comparing the two subplots of Fig. 19, noticeable differences in both fields can be observed. The effects of azimuthal coupling are evident. Indeed, when azimuthal coupling is taken into account in the calculation, the acoustic energy is horizontally refracted by the sidewalls of the canyon and gets channeled in the y direction along the

canyon axis. Note that both $N \times 2D$ and 3D solutions are symmetric about the along-canyon direction.

Figure 20 shows transmission loss-versus-range curves at $z = 30$ m and $\theta = 90^\circ$ (along the canyon axis) corresponding to 3D solutions obtained with various paraxial approximations in azimuth. Also shown on the same plot is the 2D solution. The comparison of the 3D solutions with the 2D solution confirms an enhancement of the acoustic level when azimuthal coupling is handled, due to the focusing of the acoustic energy along the canyon axis. There are also some differences between the two 3D PE solutions. The validity of the narrow-angle approximation in azimuth is subject to discussion for the present test case since, as shown in Fig. 20, using a Padé 1 paraxial approximation in azimuth changes the solution. It is worth mentioning that no change in the solution was observed for increasing values of m_p . How-

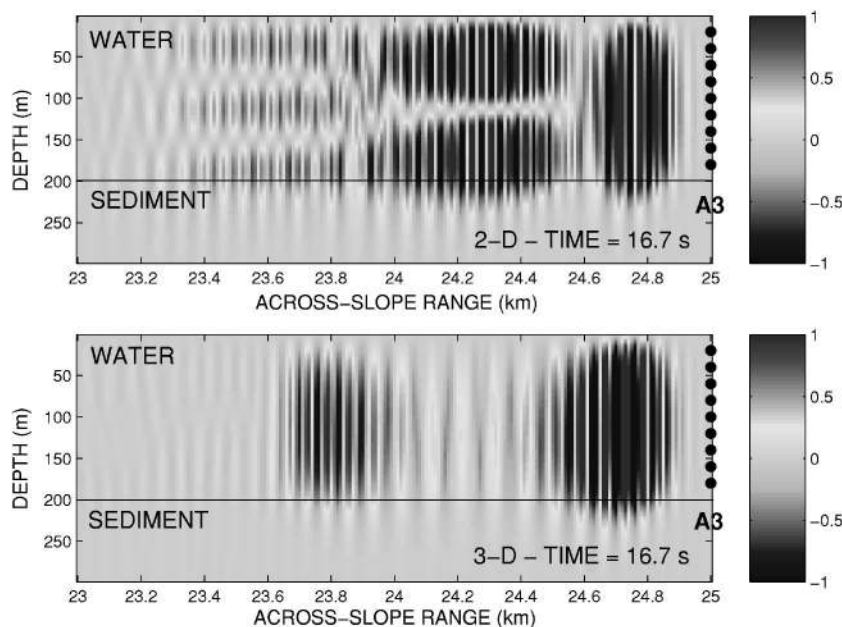


FIG. 18. Snapshots of the propagating pulse for test case A at $t = 16.7$ s: (upper) 2D calculation and (lower) 3D calculation.

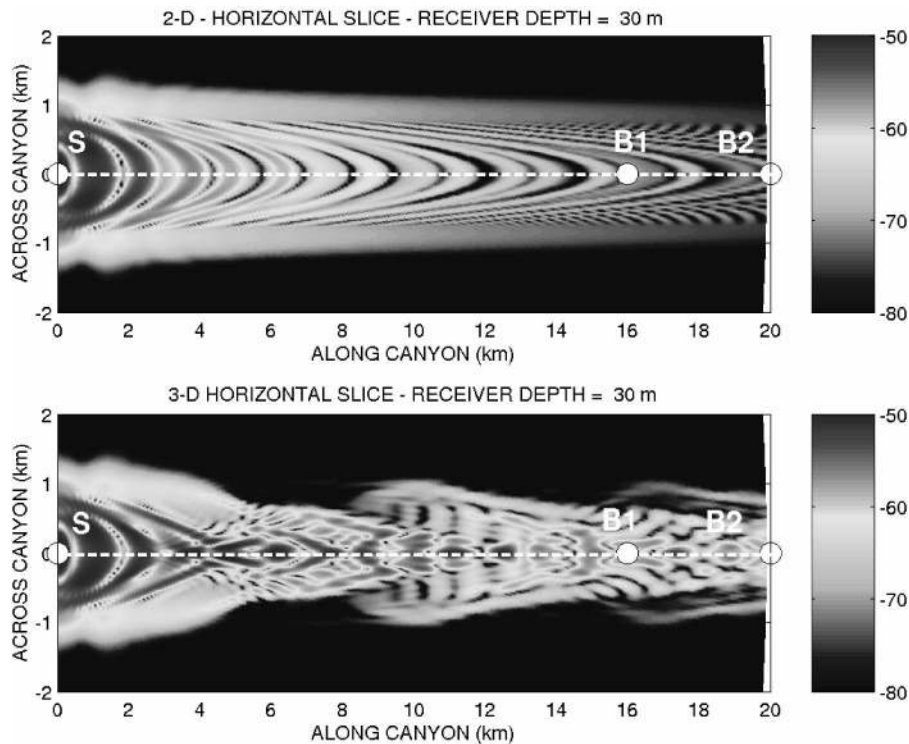


FIG. 19. Transmission loss (in dB re 1 m) at 25 Hz at a depth of 30 m for test case B corresponding to $N \times 2D$ (upper subplot) and 3D (lower subplot) PE calculations. For each calculation, the modal sum was used as a starting field. The canyon axis is indicated by a dashed white line.

ever, the error between the 3D PE solution and the exact solution can not be quantified since there is no reference solution available for this test case.

B. Modal initialization results

In order to characterize the 3D effects present in the canyon, the three propagating modes were excited individually at the source location, and propagated outward in range. For each modal initialization, the reference sound speed was selected equal to the phase speed of the m th mode. Figure 21

shows the gray-scale TL plots (horizontal slices at constant depth $z = 30$ m) obtained initializing the 3D PE model using mode 1, mode 2, and mode 3. Vertical cross sections of the 3D PE solutions are shown in Fig. 22. Figure 23 shows the modal ray diagrams for each omnidirectional modal initialization. Characteristics of the modal rays that connect the source S with one of the two arrays B1 and B2, are listed in Table II.

By comparing the results shown in Figs. 21 and 23, the solutions obtained using the PE approach and the adiabatic modal ray theory are satisfactorily in good agreement. The effects of the 3D varying bathymetry on the different modal propagations are now evident. For each propagating mode, the focusing of the energy along the canyon axis is repetitive in range and, as expected, is more pronounced for higher modes than for lower modes. Indeed, three distinct focusing zones are detected for mode 1, four distinct focusing zones for mode 2, and five distinct focusing zones for mode 3. For each propagating mode, the focusing-zone width (along the canyon axis) increases with zone number. As a result, two consecutive focusing zones may overlap at sufficiently large ranges (whose values depend on mode number) from the source along the canyon axis, and, thus, become indistinguishable. For example, for mode 1, the third focusing zone overlaps with the second one near $r \approx 19.5$ km along the canyon axis, and, for mode 2, the fourth focusing zone overlaps with the third one near $r \approx 17.5$ km along the canyon axis. Unlike test case A, no shadow zone is observed along the canyon axis. Besides, the 3D effects are more pronounced for test case B than for test case A. For example, the onset of mode 1 interference pattern along the canyon axis appears sooner in range for test case B (at $r \approx 6.5$ km) than for test case A (at $r \approx 17.5$ km).

Modes 1, 2, and 3 are present at receiver arrays B1 and

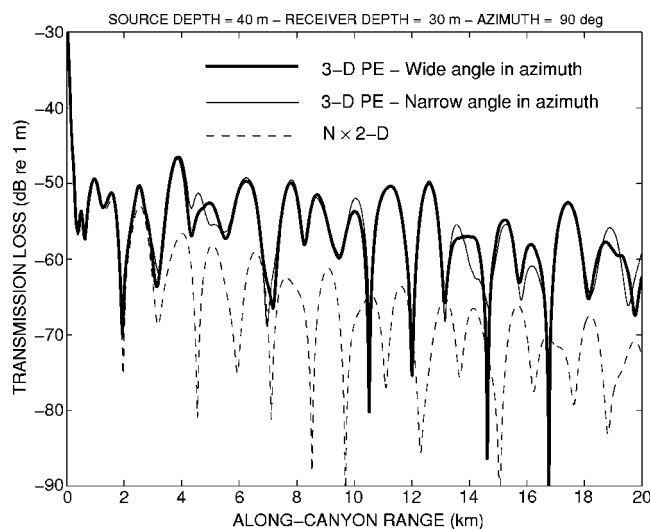


FIG. 20. $N \times 2D$ and 3D transmission loss (in dB re 1 m) comparisons at 25 Hz at a receiver depth of 30 m along a 200 m isobath along the canyon axis for test case B. The thin dashed curve is a 2D PE calculation. The two solid curves are 3D PE calculations with three Padé terms in depth and with a narrow angle (thin solid curve) or a wide-angle (bold solid curve, $m_p = 1$) approximation in azimuth. For each of the three calculations, the Greene's source was used as a starting field.

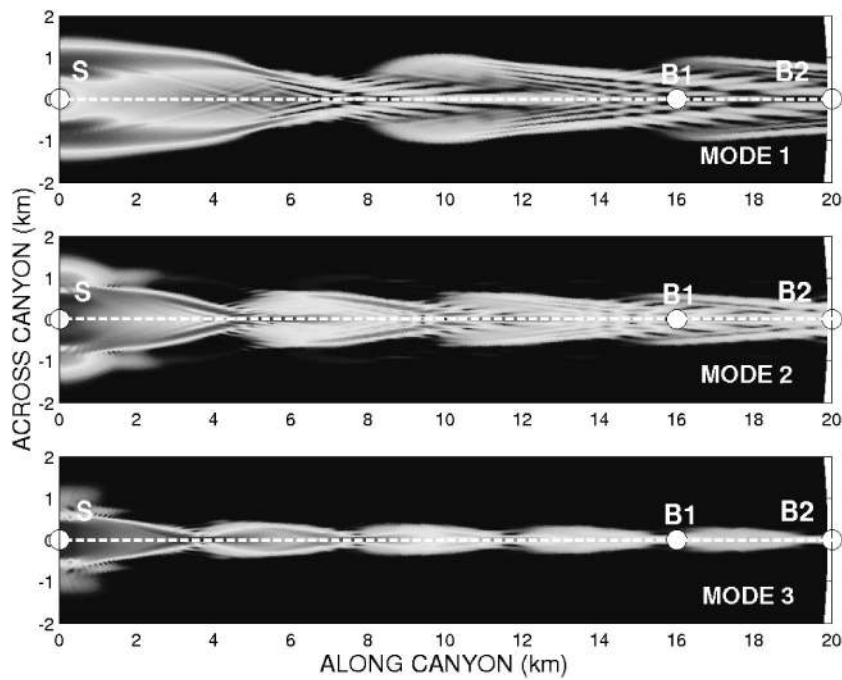


FIG. 21. Transmission loss (in dB re 1 m) at 25 Hz at a depth of 30 m for test case B corresponding to 3D PE calculations and different omnidirectional mode excitations. From top to bottom: mode 1, mode 2, and mode 3.

B2. This observation is coherent with the fact that there is no shadow zone along the canyon axis. Both receiver arrays B1 and B2 lie in the multiple mode arrival area of each of the three propagating modes, the number of eigenrays depending on both the mode number and the receiver array (see Table II). There are three modal ray paths connecting S and B1 for mode 1, the first one corresponding to $\phi_0 = 0^\circ$ (the direct path), and the two other ones corresponding to a pair of eigenrays with initial launch angles $\phi_0 = \pm 15.4^\circ$. Similarly, there are three modal ray paths connecting S and B1 for

mode 2, the direct path and a pair of eigenrays with initial launch angles $\phi_0 = \pm 13.8^\circ$. On the other hand, there are five modal ray paths connecting S and B1 for mode 3, the first one corresponding to the direct path, and the other ones to two distinct pairs of eigenrays with initial launch angles $\phi_0 = \pm 9.5^\circ$ and $\phi_0 = \pm 16^\circ$. For receiver array B2, there are one direct path and two pairs of eigenrays for each of the three propagating modes. Anticipating the analysis presented in the next section, multiple arrivals (not necessarily distinct in time) for each of the three propagating modes on both

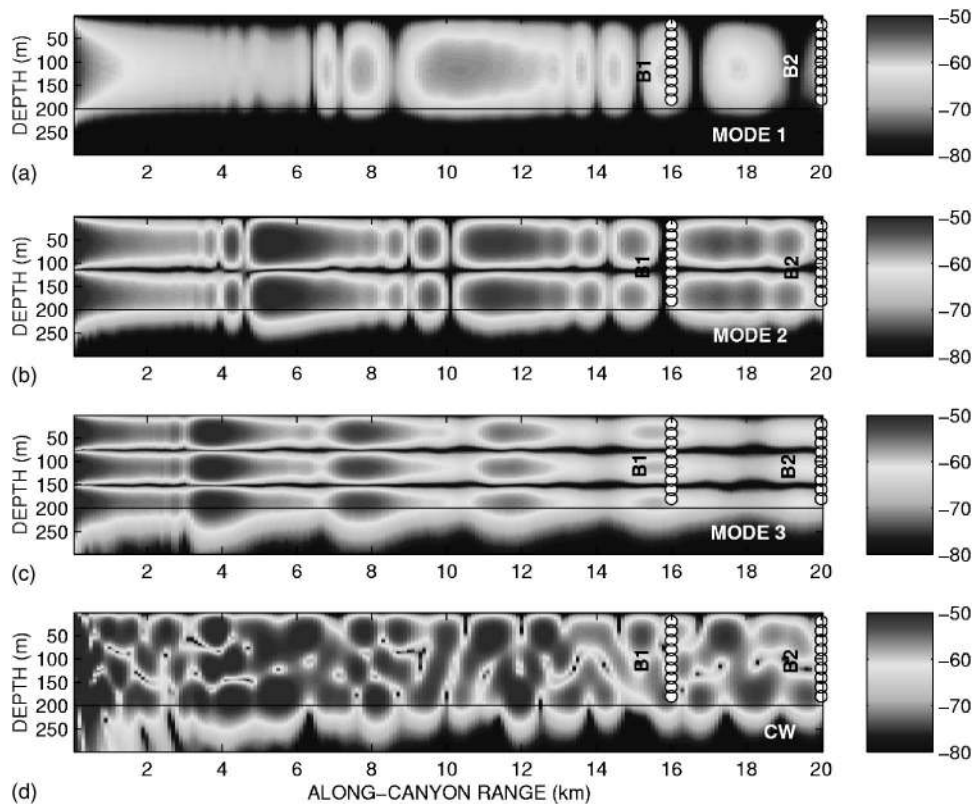


FIG. 22. 3D transmission loss (in dB re 1 m) at 25 Hz for test case B (vertical slices along the canyon axis) corresponding to 3D PE calculations and (a) mode 1, (b) mode 2, (c) mode 3, and (d) Greene's source excitations.

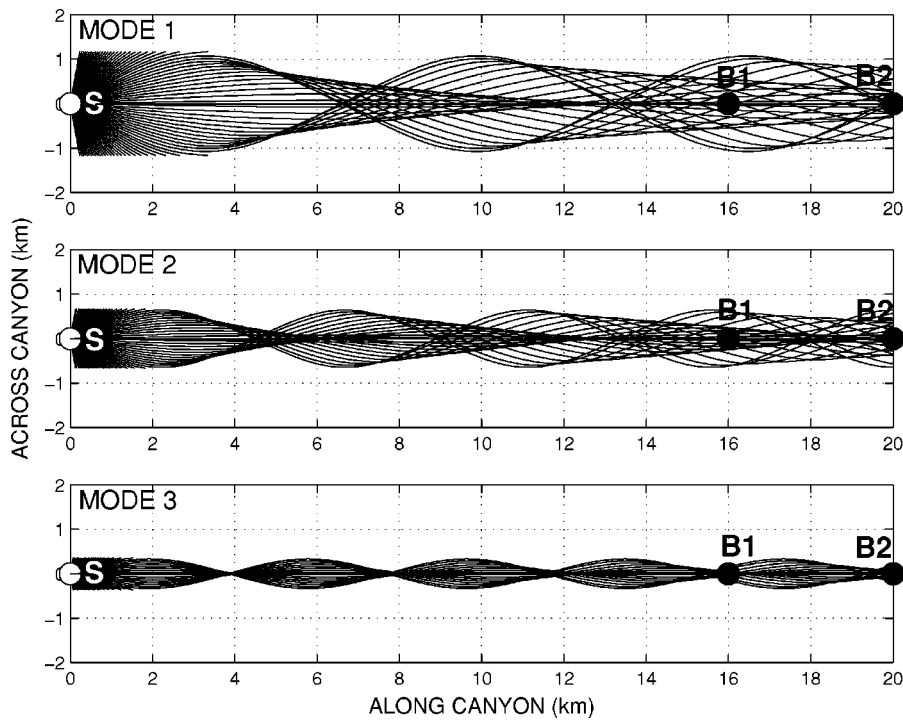


FIG. 23. Modal ray diagrams (top view) for test case B, obtained solving the differential equation given in (36) for $-90^\circ < \phi_0 < 90^\circ$. From top to bottom: mode 1, mode 2, and mode 3.

receiver arrays B1 and B2 can be predicted. More precisely, two mode 1 arrivals, two mode 2 arrivals, and three mode 3 arrivals are expected on B1. Three arrivals for each of the propagating modes are expected on B2. On the contrary, any azimuthally uncoupled model should predict only one single arrival (the direct path) for each of the three propagating modes.

C. Broadband results

Let us turn now to the analysis of the acoustic problem involving the broadband source signal given by Eq. (35). The signal arrivals on the two vertical arrays B1 and B2 were calculated. The calculations were carried out using t_{\min}

TABLE II. Characteristics (for a 25 Hz cw point source, test case B) of the modal rays launched from the source S and connected with one of the two arrays B1 and B2. The angle ϕ_0 denotes the initial launch angle ($\phi_0 = 0^\circ$ points along the canyon axis) of the modal eigenray, and L_{m,ϕ_0} denotes the length of the modal eigenray path Γ_{m,ϕ_0} .

Array	Mode m	ϕ_0 (deg)	L_{m,ϕ_0} (m)
B1	1	0	16 000
B1	1	± 15.4	16 360
B1	2	0	16 000
B1	2	± 13.8	16 258
B1	3	0	16 000
B1	3	± 9.5	16 112
B1	3	± 16	16 315
B2	1	0	20 000
B2	1	± 9	20 138
B2	1	± 23	21 050
B2	2	0	20 000
B2	2	± 2	20 005
B2	2	± 16.5	20 476
B2	3	0	20 000
B2	3	± 9.5	20 140
B2	3	± 16	20 394

$= 10.6$ s and $t_{\min} = 13$ s for receiver arrays B1 and B2 respectively, and, as in test case A, a time window of length $T = 7$ s with 4096 points in the DFT algorithm. This required running the 3D PE model at 281 discrete frequencies within the frequency band 5–45 Hz. For each frequency-domain calculation, $\Delta r = \lambda/6$, $\Delta z = \lambda/60$. The number M of discrete points in the azimuthal direction was obtained by linearly interpolating between $M = 576$ at $f = 5$ Hz and $M = 5184$ at $f = 45$ Hz, which gave $M = 2880$ at $f = 25$ Hz. The 3D PE marching algorithm was initialized at $r = 0$ using the Greene's source. Three Padé terms in depth (i.e., $n_p = 3$) and one Padé term in azimuth (i.e., $m_p = 1$) were used.

The signals received on vertical array B1 at a specific depth of 20 m corresponding to 2D and 3D computations are shown in Fig. 24. Both solutions were multiplied by the same factor $r_{B1} = 16000$ m to compensate for spherical spreading. As expected, due to the focusing of the energy along the canyon axis, the amplitude of the 3D solution is significantly higher than the amplitude of the 2D solution. The signal arrivals on vertical arrays B1 and B2 obtained using 3D calculation are displayed in Figs. 25 and 26, respectively. For comparison, the signals obtained using 2D calculation are also displayed. The two signals marked with arrows in Fig. 25 correspond to the ones shown in Fig. 24. For both vertical arrays B1 and B2, the 2D results (see first columns of Figs. 25 and 26) clearly show that the propagating signal splits up in three distinct wave packets which correspond to the signals carried by the three propagating modes of the waveguide. The 2D results are similar to that obtained in test case A. On the other hand, the modal structure of the 3D results is much more complicated (see second columns of Figs. 25 and 26). Indeed, though the first wave packet can clearly be attributed to the first arrival of mode 1, the rest of the received signals does not clearly show any modal structure. One way to discriminate the multiple arrivals of one

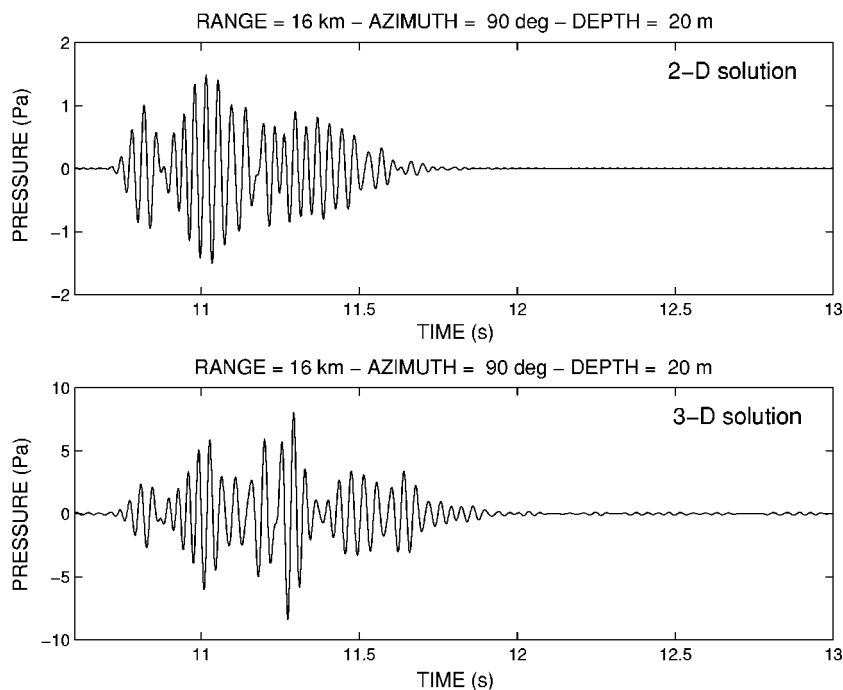


FIG. 24. Comparison of broadband pulse solutions for test case B and array B1 at a depth of 20 m: (upper) 2D calculation and (lower) 3D calculation.

mode from the multiple arrivals of the two other modes consists in initializing (in the Fourier domain) the PE model by only one single mode (if present) at each single discrete frequency, instead of initializing by the Greene's source (for which all the propagating modes are excited simultaneously). The results obtained by initializing separately by mode 1, by mode 2, and by mode 3, are displayed, respectively, in the first, second, and third columns of Figs. 27 and 28. They confirm multiple arrivals for each of the three propagating modes on receiver arrays B1 and B2. Note that multiple arrivals of the same mode can be well separated in time. For

example, this is the case for the two distinct arrivals of mode 1 on B1 (see first column of Fig. 27) and for the two distinct (though very close in time but still distinguishable) arrivals of mode 2 on B1 (see second column of Fig. 27). This is also the case for the three distinct arrivals of mode 1 on B2 (see first column of Fig. 28). On the contrary, the multiple arrivals of mode 3 on B1 and B2 (see third columns of Figs. 27 and 28) are very close in time. The wave packets observed correspond to the merger of the three distinct arrivals of the same mode. They thus appear more dispersed in time than the single mode 3 arrival obtained using a 2D model. Again,

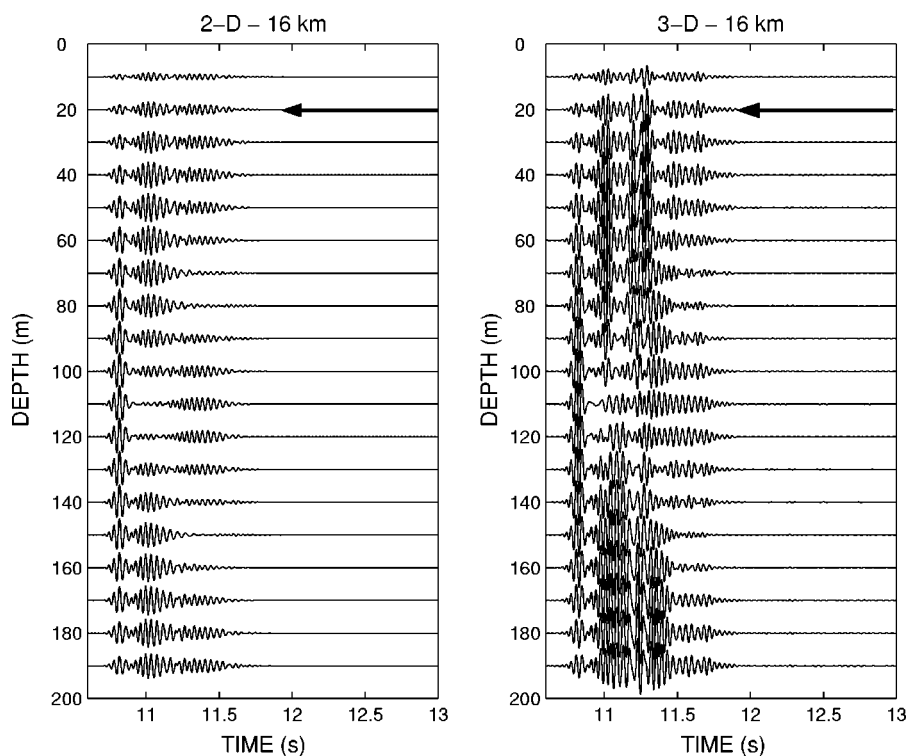


FIG. 25. Stacked time series vs depth corresponding to vertical array B1 (placed along the canyon axis at a distance of 16 km) obtained using 2D computation (left column) and 3D computation (right column).

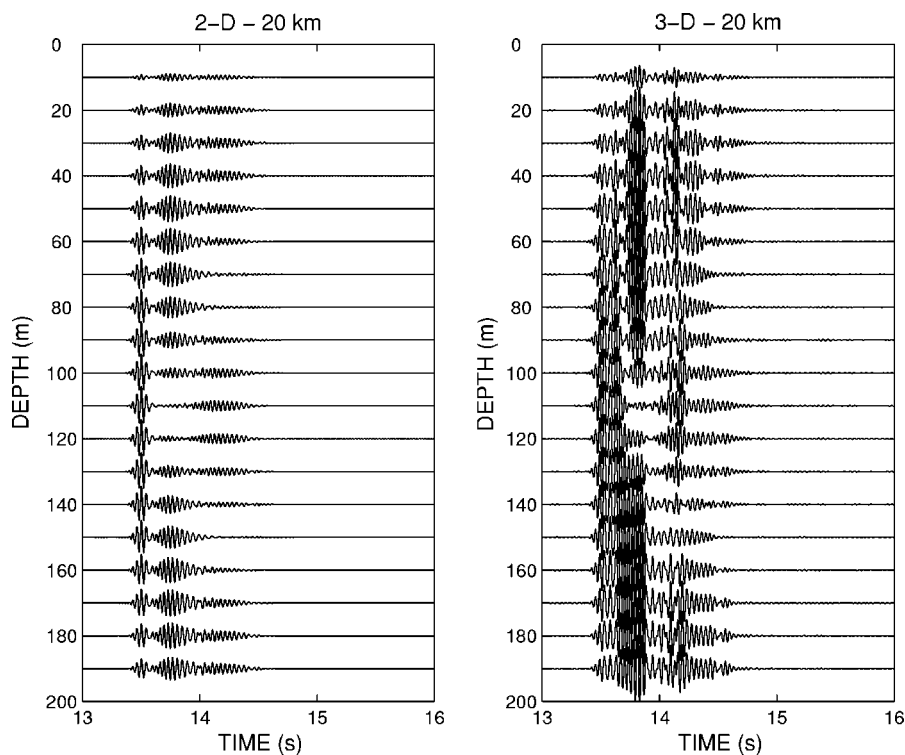


FIG. 26. Stacked time series vs depth corresponding to vertical array B2 (placed along the canyon axis at a distance of 20 km) obtained using 2D computation (left column) and 3D computation (right column).

all these observations are consistent with the predictions of the previous section.

VI. CONCLUSION

In this paper, the propagation of a broadband acoustic pulse with a central frequency of 25 Hz and a bandwidth of 40 Hz in three-dimensional shallow water waveguides was studied. The 3D ASA benchmark problem, and a variant of

the original SWAM'99 Gaussian canyon test case were investigated. Both test cases were treated following the same approach. First, the acoustic problem was simplified to an harmonic point source emitting at 25 Hz. Results for both point source and modal initializations were obtained. Solutions from the 3D PE model were compared with the predictions from a 3D adiabatic modal theory. Good agreement was obtained between the two models for both test cases. For the

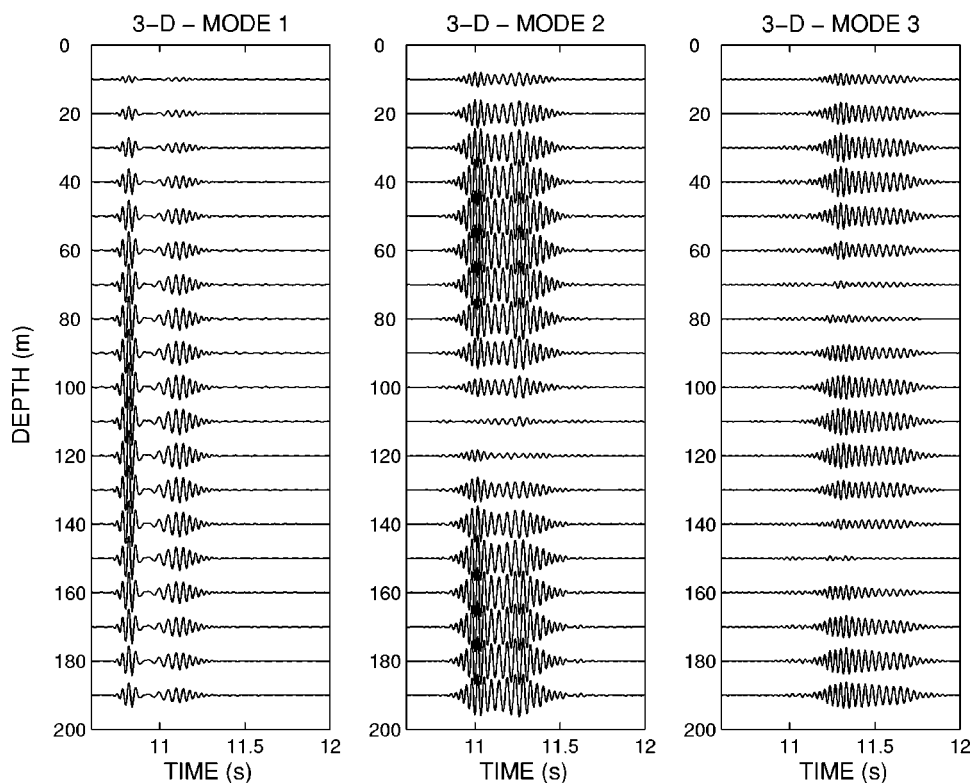


FIG. 27. Stacked time series vs depth corresponding to vertical array B1 (placed along the canyon axis at a distance of 16 km) obtained using 3D computations. The signals have been obtained initializing the PE model by mode 1 (left), by mode 2 (middle), and by mode 3 (right).

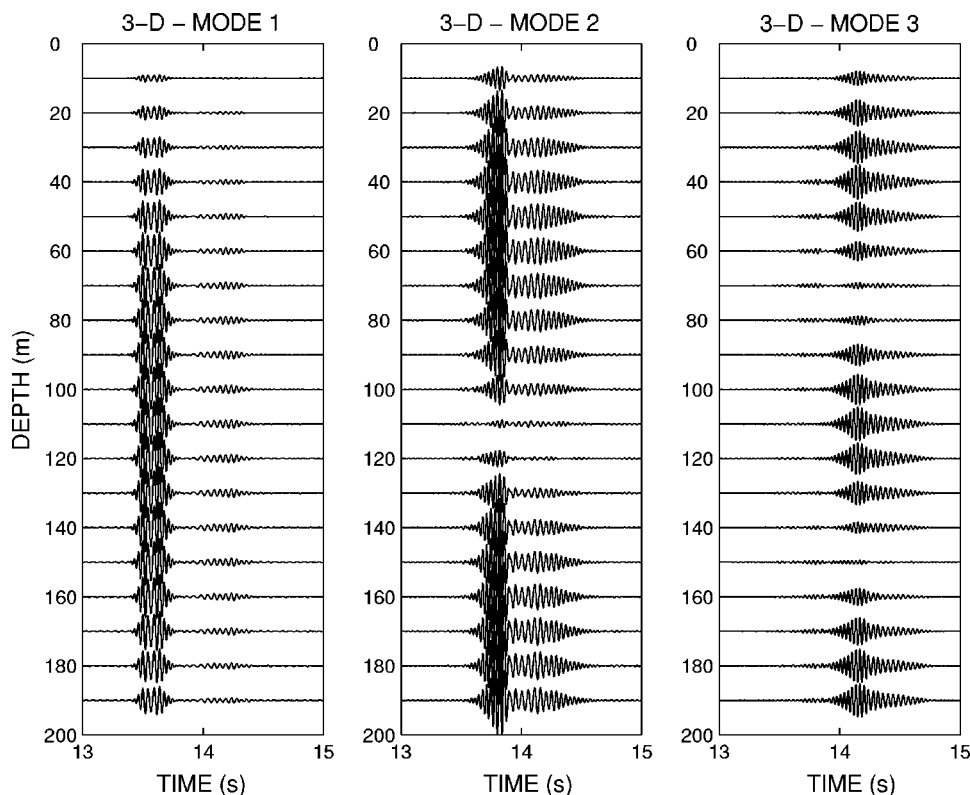


FIG. 28. Stacked time series vs depth corresponding to vertical array B2 (placed along the canyon axis at a distance of 20 km) obtained using 3D computations. The signals have been obtained initializing the PE model by mode 1 (left), by mode 2 (middle), and by mode 3 (right).

3D ASA benchmark problem, comparisons of 3D PE solutions with a reference analytical solution (based on the image method) were made, hence validating the 3D PE model for this test case. Unfortunately, no reference solution was available for the Gaussian canyon test case. The signals received by vertical arrays located far from the source were calculated. For the 3D ASA wedge problem, multiple mode arrival times (e.g., two distinct mode 1 arrivals on A2 and A3, and only one single mode 1 arrival on A1) or modal shadow zones (e.g., no mode 3 arrival on each of the vertical arrays A1, A2, and A3) were observed. For the Gaussian canyon test case, the analysis of the signals received by two vertical arrays B1 and B2 located along the canyon confirmed an increase of the acoustic level due to energy focusing along the canyon axis. Multiple mode arrivals on each of the vertical arrays for each of the three propagating modes were observed. No modal shadow zone was observed along the canyon axis. For both test cases, geometrical dispersion of the propagating modes was consistent with results obtained for a 25 Hz cw point source.

These phenomena are typical of shallow water oceanic environments in the presence of a sloping bottom. They have already been described numerically for a 3D wedge-shaped waveguide using a code based on the image source method.¹⁶ Note that the latter code was limited to specific oceanic environments. The main advantage of using a 3D PE model is that it can be applied quite generally and is thus not restricted to a specific acoustic problem. *A priori*, the methodology that has been used to analyze the two acoustic problems, the 3D wedge and the 3D Gaussian canyon, could be applied in future for investigating any other shallow water acoustic problem. Nevertheless, the modeler should be wary when performing numerical simulations with a 3D PE model. For

instance, it is important to keep in mind that any existing and available 3D PE based model is only an approximate model (though general) and is limited in its ability to handle horizontal refraction. Indeed, though the 3D PE model used in this paper, 3DWAPE, has a wide-angle capability along the azimuthal direction (comparisons for the 3D wedge seem to favor the use of the azimuthal wide-angle approximation), it does not strictly speaking have a wide-angle capability since the cross-derivative terms present in $O(\mathcal{X})$ are not taken into account in the modeling. This point was discussed in detail in this paper. The influence of handling cross-derivative terms is not known. Efforts to incorporate these terms in 3DWAPE as well as in a 3D version of the Monterey-Miami Parabolic Equation model developed by Smith⁹ are currently under way. Another issue that can be addressed when one is interested with pulse propagation in shallow water environments is the following: if shear waves are present in the bottom, do they modify the three-dimensional effects described in this paper, and if so, by how much? This question has not been addressed in this present work since the 3D model used could not handle shear waves. It is left for future works.

ACKNOWLEDGMENTS

The author wishes to thank Evan Westwood (Applied Research Laboratories, University of Austin, Texas, USA) who provided numerical data. Part of this work has been presented at the 6th International Conference on Theoretical and Computational Acoustics held in August 2003 in Hawaii. The author is very grateful to Michael Taroudakis (Department of Mathematics, University of Crete, Greece) for his

invitation to the ICTCA'03 conference and to Finn Jensen (Saclant Undersea Research Center, Italy) for his encouragement to write the present paper.

- ¹R. Doolittle, A. Tolstoy, and M. Buckingham, "Experimental confirmation of horizontal refraction of CW acoustic radiation from a point source in a wedge-shaped ocean," *J. Acoust. Soc. Am.* **83**, 2117–2125 (1988).
- ²S. Glegg, G. Deane, and I. House, "Comparison between theory and model scale measurements of the three-dimensional sound propagation in a shear supporting penetrable wedge," *J. Acoust. Soc. Am.* **94**, 2334–2342 (1993).
- ³C. Chen, J.-T. Lin, and D. Lee, "Acoustic three-dimensional effects around Taiwan strait: Computational results," *J. Comput. Acoust.* **7**, 15–26 (1999).
- ⁴M. Buckingham, "Theory of three-dimensional acoustic propagation in a wedgelike ocean with a penetrable bottom," *J. Acoust. Soc. Am.* **82**, 198–210 (1987).
- ⁵G. Deane and M. Buckingham, "An analysis of the three-dimensional sound field in a penetrable wedge with a stratified fluid or elastic basement," *J. Acoust. Soc. Am.* **93**, 1319–1328 (1993).
- ⁶D. Lee, G. Botseas, and W. Siegmann, "Examination of three-dimensional effects using a propagation model with azimuth-coupling capability (FOR3D)," *J. Acoust. Soc. Am.* **91**, 3192–3202 (1992).
- ⁷G. Brooke, D. Thomson, and G. Ebbeson, "PECAN: A Canadian parabolic equation model for underwater sound propagation," *J. Comput. Acoust.* **9**, 69–100 (2001).
- ⁸J. Fawcett, "Modeling three-dimensional propagation in an oceanic wedge using parabolic equation methods," *J. Acoust. Soc. Am.* **93**, 2627–2632 (1993).
- ⁹K. Smith, "A three-dimensional propagation algorithm using finite azimuthal aperture," *J. Acoust. Soc. Am.* **106**, 3231–3239 (1999).
- ¹⁰M. Collins and S. Ching-Bing, "A three-dimensional parabolic equation model that includes the effects of rough boundaries," *J. Acoust. Soc. Am.* **87**, 1104–1109 (1990).
- ¹¹A. Tolstoy, "3-D propagation issues and models," *J. Comput. Acoust.* **4**, 243–271 (1996).
- ¹²D. Lee, A. Pierce, and E.-C. Shang, "Parabolic equation development in the twentieth century," *J. Comput. Acoust.* **8**, 527–637 (2000).
- ¹³F. Sturm and J. Fawcett, "On the use of higher-order azimuthal schemes in 3-D PE modelling," *J. Acoust. Soc. Am.* **113**, 3134–3145 (2003).
- ¹⁴F. Jensen and C. Ferla, "Numerical solutions of range-dependent benchmark problems in ocean acoustics," *J. Acoust. Soc. Am.* **87**, 1499–1510 (1990).
- ¹⁵F. Sturm, "Examination of signal dispersion in a 3-D wedge-shaped waveguide using 3DWAPE," *Acta Acustica united with Acustica* **88**, 714–717 (2002).
- ¹⁶E. Westwood, "Broadband modeling of the three-dimensional penetrable wedge," *J. Acoust. Soc. Am.* **92**, 2212–2222 (1992).
- ¹⁷A. Tolstoy, K. Smith, and N. Maltsev, "The SWAM'99 workshop—An overview," *J. Comput. Acoust.* **9**, 1–16 (2001).
- ¹⁸J. Arvelo and A. Rosenberg, "Three-dimensional effects on sound propagation and matched-field processor," *J. Comput. Acoust.* **9**, 17–39 (2001).
- ¹⁹F. Jensen, W. Kuperman, M. Porter, and H. Schmidt, *Computational Ocean acoustics*, AIP Series in Modern Acoustics and Signal Processing (AIP, New York, 1994).
- ²⁰F. Jensen, C. Ferla, P. Nielsen, and G. Martinelli, "Broadband signal simulation in shallow water," *J. Comput. Acoust.* **11**, 577–591 (2003).
- ²¹F. Tappert, "Parabolic equation modeling with the split-step Fourier algorithm in four dimensions," *J. Acoust. Soc. Am.* **103**, 2090:4aUW6 (1998).
- ²²M. Porter, "The time-marched fast-field program (FFP) for modeling acoustic pulse propagation," *J. Acoust. Soc. Am.* **87**, 2013–2023 (1990).
- ²³J. Murphy, "Finite-difference treatment of a time-domain parabolic equation: Theory," *J. Acoust. Soc. Am.* **77**, 1958–1960 (1985).
- ²⁴B. McDonald and W. Kuperman, "Time domain formulation for pulse propagation including nonlinear behavior at a caustic," *J. Acoust. Soc. Am.* **81**, 1406–1417 (1987).
- ²⁵M. Collins, "The time-domain solution of the wide-angle parabolic equation including the effects of sediment dispersion," *J. Acoust. Soc. Am.* **84**, 2114–2125 (1988).
- ²⁶M. Collins, "Applications and time-domain solution of higher-order parabolic equations in underwater acoustics," *J. Acoust. Soc. Am.* **86**, 1097–1102 (1989).
- ²⁷A. Bamberger, B. Engquist, L. Halpern, and P. Joly, "Higher order paraxial wave equation approximations in heterogeneous media," *SIAM (Soc. Ind. Appl. Math.) J. Appl. Math.* **48**, 129–154 (1988).
- ²⁸M. Collins, "Higher order Padé approximations for accurate and stable elastic parabolic equations with application to interface wave propagation," *J. Acoust. Soc. Am.* **89**, 1050–1057 (1991).
- ²⁹F. Tappert, "The parabolic approximation method," in *Wave propagation and underwater acoustics*, Lecture notes in Physics Vol. 70, edited by J. B. Keller and J. S. Papadakis (Springer, Berlin, 1977), pp. 224–287.
- ³⁰G. Botseas, D. Lee, and D. King, "FOR3D: A computer model for solving the LSS three-dimensional wide angle wave equation," Technical report, Naval Underwater Systems Center, Technical Document 7934, New London, CT.
- ³¹F. Sturm, "Modélisation mathématique et numérique d'un problème de propagation en acoustique sous-marine: prise en compte d'un environnement variable tridimensionnel," Ph.D. thesis, Université de Toulon et du Var, 1997.
- ³²F. Sturm, J. Fawcett, and F. Jensen, "Benchmarking two three-dimensional parabolic equation methods," *J. Acoust. Soc. Am.* **103**, 2090:4aUW5 (1998).
- ³³F. Sturm and J. Fawcett, "Numerical simulation of the effects of the bathymetry on underwater sound propagation using three-dimensional parabolic equation models," Technical report, SM-342, SACLANT Undersea Research Centre, La Spezia, Italy.
- ³⁴W. Siegmann and D. Lee, "Aspects of three-dimensional parabolic equation computations," *Comput. Math. Appl.* **11**, 853–862 (1985).
- ³⁵W. Siegmann, G. Kriegsmann, and D. Lee, "A wide-angle three-dimensional parabolic wave equation," *J. Acoust. Soc. Am.* **78**, 659–664 (1985).
- ³⁶D. Lee and W. Siegmann, "A mathematical model for the 3-dimensional ocean sound propagation," *Math. Modelling* **7**, 143–162 (1986).
- ³⁷M. Collins, "The split-step Padé solution for the parabolic equation method," *J. Acoust. Soc. Am.* **93**, 1736–1742 (1993).
- ³⁸C. F. Chen, Y.-T. Lin, and D. Lee, "A three-dimensional azimuthal wide-angle model," *J. Comput. Acoust.* **7**, 269–288 (1999).
- ³⁹E. Westwood, "Complex ray solutions to the 3-D wedge ASA benchmark problems," *J. Acoust. Soc. Am.* **109**, 2333:2aAOa6 (2001).
- ⁴⁰R. Greene, "The rational approximation to the acoustic wave equation with bottom interaction," *J. Acoust. Soc. Am.* **76**, 1764–1773 (1984).
- ⁴¹H. Weinberg and R. Burridge, "Horizontal ray-theory for ocean acoustics," *J. Acoust. Soc. Am.* **55**, 63–79 (1974).